Theoretical model of membrane protrusions driven by curved active proteins

Yoav Ravid[1]*, Samo Penič[2], Yuko Mimori-Kiyosue[3]†,
Shiro Suetsugu[4,5,6], Aleš Iglič[2] and Nir S. Gov[1]*

[1]Department of Chemical and Biological Physics, Weizmann Institute of Science, Rehovot, Israel,
[2]Laboratory of Physics, Faculty of Electrical Engineering, University of Ljubljana, Ljubljana, Slovenia,
[3]Laboratory for Molecular and Cellular Dynamics, RIKEN Center for Biosystems Dynamics Research,
Minatojima-minaminachi, Kobe, Hyogo, Japan, [4]Division of Biological Science, Graduate School of
Science and Technology, Nara Institute of Science and Technology, Nara, Japan, [5]Data Science Center,
Nara Institute of Science and Technology, Ikoma, Japan, [6]Center for Digital Green-innovation, Nara
Institute of Science and Technology, Ikoma, Japan

Eukaryotic cells intrinsically change their shape, by changing the composition of their membrane and by restructuring their underlying cytoskeleton. We present here further studies and extensions of a minimal physical model, describing a closed vesicle with mobile curved membrane protein complexes. The cytoskeletal forces describe the protrusive force due to actin polymerization which is recruited to the membrane by the curved protein complexes. We characterize the phase diagrams of this model, as function of the magnitude of the active forces, nearest-neighbor protein interactions and the proteins' spontaneous curvature. It was previously shown that this model can explain the formation of lamellipodia-like flat protrusions, and here we explore the regimes where the model can also give rise to filopodia-like tubular protrusions. We extend the simulation with curved components of both convex and concave species, where we find the formation of complex ruffled clusters, as well as internalized invaginations that resemble the process of endocytosis and macropinocytosis. We alter the force model representing the cytoskeleton to simulate the effects of bundled instead of branched structure, resulting in shapes which resemble filopodia.

KEYWORDS

cell membrane, curved inclusions, Monte-Carlo simulations, closed vesicle shapes, cell motility, filopodia

1 Introduction

Cells in our body have different shapes depending on their function, and they control their shapes by exerting forces on the flexible plasma membrane (Frey and Idema, 2021). These forces are mostly due to the underlying cytoskeleton, dominated by the cortical actin network. The actin polymerization near the membrane exerts protrusive forces that can give rise to cellular protrusions, such as filopodia and lamellipodia (Mattila and Lappalainen, 2008). The control of the actin polymerization in space and time is provided by a host of proteins that nucleate actin polymerization where and when it is needed, and are in turn controlled by different signalling cascades. One mechanism for controlling the spatial pattern of actin polymerization on the membrane, is to couple the actin nucleation to curved membrane components (CMCs), that are both bending locally the membrane and are sensitive to the local membrane curvature. Bending the membrane can occur due to
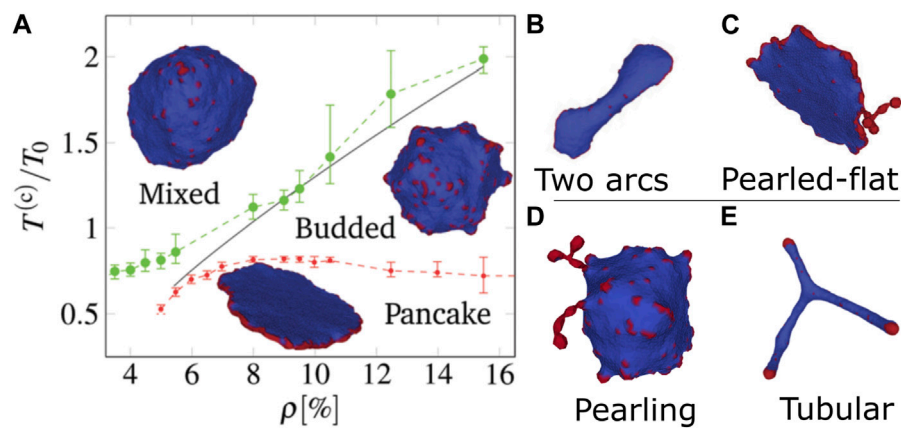
FIGURE 1
Phases of vesicle shapes driven by curved active CMC, as obtained in Fošnarič (2019). **(A)** Phase diagram in the temperature-density plane: mixed (gas), budded, and flattened (pancake). The gas phase is dominated by entropy, hence appears at either high temperatures or low densities. The pancake phase is dominated by having favorable binding and bending energy, where the active forces are all radial and stabilize the flat shape. This phase requires large stable CMC cluster, and so can only appear at low temperatures. The budded phase appears between the two other phases. At a CMC density that is lower than the minimal value needed for a closed circular rim, the pancake shape changes to **(B)** a two-arcs phase, while when the CMC concentration is very high the pancake forms pearled extensions that contain the surplus CMC **(C)**. There are two other phases in different regimes: **(D)** The pearling phase appears at higher CMC density, where most of the CMC aggregate into long necklace-like clusters that minimize the protein-protein binding energy (phase-separation of CMC), and **(E)** highly-elongated (tubular) phase for flat CMCs, where large CMC caps can exert a strong force that pulls out elongated tubes. Reproduced with permission from Fošnarič (2019): Figures 4C, 7D, 7SI.

adsorption of specialized proteins that have a curved shape (such as BAR domain proteins (Simunovic et al., 2015)), as well as by formation of nanodomains of different lipid composition and polymerization of membrane-bound filaments (Zimmerberg and Kozlov, 2006; McMahon and Boucrot, 2015; Drab et al., 2023). For the purpose of our model, we do not need to specify the exact molecular components of the CMC, as long as they are curved and that they can also nucleate actin polymerization at the membrane. Nucleators of actin polymerization, such as WAVE, have been associated with curved membrane complexes (Begemann et al., 2019; Pipathsouk et al., 2021).

This coupling was shown theoretically to give rise to positive and negative feedbacks (Gov, 2018), that can result in pattern formation in both the spatial distribution of the actin nucleators (recruited by the CMCs) and the membrane shape. This coupling between curvature and active protrusive forces was explored for a limited regime of parameters in Fošnarič (2019). Experimental evidence for this coupling between CMC and protrusive forces has been accumulated in the context of lamellipodia (Begemann et al., 2019; Pipathsouk et al., 2021) and filopodia (Scita et al., 2008; Ahmed et al., 2010; Vaggi et al., 2011; Mancinelli et al., 2021; Fox et al., 2022; Tsai et al., 2022; Lee et al., 2023) formation.

A summary of the vesicle shapes that we found in Fošnarič (2019) are shown in Figure 1, explored as function of temperature and CMC density (Figure 1A). The main phases which were identified are (Drab et al., 2023):

- Diffused CMC-gas phase, where CMC are dispersed as entropy dominates over bending and binding energies.
- Budded phase, where binding and bending leads to CMC forming hemispherical clusters at the CMC spontaneous curvature.

- Flattened "pancake" phase, where the active forces push the CMC outwards, leading to a large CMC cluster along the rim, with two flat bare membrane disc regions. Low temperature is required to prevent lateral membrane fluctuations and thermal diffusion of the CMC from breaking up the rim cluster.

The pancake phase is quite dynamic, and tends to form "ruffles" along the edges. With insufficient density of CMC, there is a "two-arc" phase with multiple flat edges connected by elongated membrane (Figure 1B). If the CMC density if high, the excess CMC form pearled structures along the rim of the pancake (Figure 1C).

When the active force is weak or zero (passive CMC), at low temperatures the system is phase-separated into energy-minimizing "pearled necklace" of CMC clusters, each at the CMC spontaneous curvature (Figure 1D). When the force is strong and the CMC have low spontaneous curvature (flat), there is a phase of highly elongated "tubular" vesicles, where CMC caps apply large forces that pull membrane tethers (tubular protrusions) (Figure 1E).

Here we expand the analysis of the coupling between the spontaneous curvature of the CMC and protrusive forces, by exploring the patterns that form as function of the natural parameters that the cell can manipulate, such as the strength of the actin-driven force, the binding strength between the CMCs and the spontaneous curvature of the CMCs. By gaining a fuller understanding of the space of shapes that this coupling can produce, we are able to explore two more complex configurations: a mixture of two CMCs of different intrinsic curvatures, and CMCs that induce aligned active forces which model the effects of actin bundling (Mellor, 2010). These more complex systems, can be compared to important biological

TABLE 1 The values of the model parameters used in the simulations, in the different figures. The energy units are $K_B T = 1$, which define the scale of f, w, κ, and the length units are $\ell_{min} = 1$, which define the scale of the vertex lattice, the force, and spontaneous curvature.

Parameter	units	Figure 1, (Fošnarič et al., 2019)	Figure 2	Figure 4A	Figure 4C	Figure 6	Figure 7	Figure 8
f	$K_B T/\ell_{min}$	1	0–1.2	0–0.5	0.5	0.2	0.2, 0.5	0.5
w	$K_B T$	1	0–4.8	2	2	2	2	2
κ	$K_B T$	20*	20	28.5	28.5	28.5	28.5	28.5
ρ	1	0%–20%	10%	20%	10%, 10%	20%	20%	10%, 10%
C_0	$1/\ell_{min}$	1 0	1	0.8	-0.75–0, 0.8	0.4	0.4, 0.1	0.8

phenomena, such as endocytosis (Doherty and McMahon, 2009) and filopodia.

2 The model

We follow the same coarse-grained continuum model used previously (Fošnarič et al., 2019) and (Sadhu et al., 2021), where the physics of the cell shape is described by differential geometry and very few energy components (Frey and Idema, 2021; Gov et al., 2023). The lipid bilayer membrane is modeled as a 2D flexible sheet, with zero spontaneous curvature, except where there are CMCs. Each CMC on the membrane surface represents a complex of proteins that have a specific spontaneous curvature. The energy of the surface is modeled by the Helfrich Hamiltonian

$$H_{bending} = \iint \frac{\kappa}{2}(C_1 + C_2 - C_0\phi)^2 dA \quad (1)$$

This penalizes (with a bending modulus of κ) deviation of the local shape of the membrane from its intrinsic natural shape: The local shape is given by the curvatures C_1 and C_2, and the preferred local shape is determined by the CMC relative lateral density ϕ and their preferred curvature C_0 and dA is infinitesimal membrane area element. To simulate, we discretize the system as a closed vesicle described by a graph V, E (vertices and edges respectively) with vertices representing small area patches of either bare lipid bilayer or CMC. Note that the simulation does not have an intrinsic length scale, however the edge length has to represent lengths larger than tens of nanometers for the coarse-grained model to be physically valid. We therefore obtain the following discretized energy

$$E = \sum_{i \in V} \frac{\kappa}{2}(2h(i) - \rho_i C_0)^2 A(i) + \sum_{\langle i,j \rangle \in E} -w\rho_i\rho_j + \sum_{i \in V} w_{ad}\,\theta(z_i - z_0) \quad (2)$$

where $\rho_i = 1$ for a CMC vertex and $\rho_i = 0$ for a bare vertex, such that the overall density of CMC is given by $\rho = \sum_{i \in V}\rho_i/N$, where $N = 4502$ is the total number of vertices in our simulations. The first term is a discretized version of the bending energy (Eq.1), $h(i)$ is the mean curvature calculated at each vertex $h = (C_1 + C_2)/2$, C_0 is the spontaneous curvature of a CMC, and $A(i)$ is the area assigned to the vertex. The second term is the CMC-CMC nearest-neighbor binding energy, going over the edges $\langle i, j \rangle$, where w is the binding energy per bond. The third term is adhesion energy of the membrane to a flat rigid surface

located at $z = z_0$, which applies to all the nodes that are within a distance of ℓ_{min} from this surface. The membrane is prevented from moving below $z_0 - \ell_{min}$.

This energy model is used in a Monte-Carlo (MC) simulation `Trisurf-ng`, described in Fošnarič (2019), where random movement of vertices and bond flips of edges are accepted if they lower the energy or according to a Boltzmann probability: $P = \exp(-\Delta E - W_i)$ where W_i represents the work done by the active forces on each node that contains a CMC, as follows

$$W_i = -f\hat{n}(i) \cdot \vec{\delta x_i} \quad (3)$$

where $\hat{n}(i)$ is the local outwards normal unit vector, and $\vec{\delta x_i}$ is the vertex displacement.

The shift in the locations of the vertices are limited such that the length of each edge remains within this range: $\ell_{min} < \ell < \ell_{max}$. The edge length and adhesion surface constraints are enforced by rejecting any MC moves which violate them. In a passive system this would lead to thermal equilibrium, but the active work term is unbounded from below, so the system is out of equilibrium. The MC simulation does not have time-scale, as it does not include the hydrodynamic flows and dissipative processes that determine the relaxation time-scales of the membrane shape changes. It does allow us to follow the shape dynamics by evolving the system along decreasing energy gradients, so the trajectory in shape space is correctly described.

The continuum model, on which our coarse-grained triangulated treatment is based, is valid for membrane lengthscales that are at least several times the membrane thickness. Therefore the length l_{min} can represent meaningfully lengths that are longer than ~ 10 nanometers. However, beyond this lower bound limitation, the lengthscales in the model are not strictly defined, and similarly the size of the whole vesicle. We therefore chose the vesicle size according to computational considerations: that is large enough to allow for accurate description of the membrane deformations, while not too large to be computationally prohibitive.

The membrane tension is not explicitly described in our model, but we do conserve the overall membrane area (approximately, less than 10% changes), so in this sense the effects of membrane tension are included. It was shown in the past that explicit tension does not change the results qualitatively (Graziano et al., 2019). We do not conserve here the volume of the vesicle, to allow the membrane to undergo large shape changes as freely as possible.

The parameters in the model, used in this paper, are given in Table 1. All the energies in the model are in units of k_BT (κ, w), while the external force f is in units of $k_BT/\ell_{\min}$.

In addition, we implement optional models of inhibition of the force on the CMC by neighbors, based on Sitarska et al. (2021) which shows different protein species can inhibit the activity of polymerization, inhibiting the actin recruitment and thus force on the CMCs. We implement a proportional inhibition, where an active (1) and inhibiting (2) CMC species exist

$$f_i^{prop} = f \frac{1}{N_{\text{neighbors}}} \sum_{\langle i,j \rangle} \left(1 - \rho_j^{(2)}\right) \qquad (4)$$

We also implement a disabling inhibition, where any inhibiting CMC species completely disables the force on it is neighbors.

$$f_i^{dis} = f \prod_{\langle i,j \rangle} \left(1 - \rho_j^{(2)}\right) \qquad (5)$$

In biological filopodia, the actin filament are known to bundle by cross-linking proteins (Faix and Rottner, 2006). Our model does not have a true representation of the cytoskeleton structure, but we can simulate this bundling by adding an alignment to the force on the active CMCs, since the shared internal actin bundle would apply a force in the same direction. This is added as an Vicsek-like interaction (Vicsek and Zafeiris, 2012)

$$\hat{f} = \frac{\hat{n}_i + s \sum_r \hat{n}_j}{\left|\hat{n}_i + s \sum_r \hat{n}_j\right|} \qquad (6)$$

The direction of force on CMC vertex i $\hat{f}_i$ is a weighted average of the normal direction plus a contribution from all the vertices j a distance r from the vertex i with a weight of s, normalized. This replaces the $\hat{n}(i)$ term in the work term i.e. the unmediated local normal. This is superficially similar to the normal Vicsek model (Vicsek and Zafeiris, 2012), where self-propelled particles similarly align their direction with neighbors, producing flocking behavior, but here the CMCs/particles are connected to each other and embedded in a 2D flexible sheet, and we use force in a MC simulation instead of velocity in a Langevin simulation.

3 Materials and methods

3.1 Computational methods

The simulations were run using trisurf-ng (Fošnarič et al., 2019) version fb86a41 ("Modeled_trisurf" branch) (see Data availability statement) with a tape file modified from the available default with the different physical parameters (see Table 1), and additional simulation running parameters of nshell = 30, MCsweeps = 50,000–200,000, iterations = 100–1,000 (depending on the desired time resolution). Each simulation with a set of parameters was ran independently ("embarrassingly parallel"), which took about 2 weeks to finish, with occasional restarts and expansion of the space limits (nxmax). The resulting VTU files were viewed and colored in ParaView, but further analysis and graph generation were done by separate python scripts.

3.2 Experimental methods

The cell culture and lattice light sheet microscopic observation U-251 cells were obtained from the Japanese Collection of Research Bioresources Cell Bank. The IRSp53 knockout (KO) cells were generated by the CRISPR/Cas9 system, as described previously (Mashiko et al., 2013). The guide RNA targeting the first exon of IRSp53 (CCATGGCGATGAAGTTCCGG) was designed using the server http://crispr.mit.edu and inserted into the pX330 vector (Mashiko et al., 2013). After transfection, the cells were cloned by monitoring the GFP fluorescence from the reporter plasmid pCAG-EGxxFP with the IRSp53 genome fragment using a fluorescence-activated cell sorter [FACSAria (BD)] (Hanawa-Suetsugu et al., 2019). The expression of GFP or GFP-IRSp53 in the IRSp53 knockout cells was performed by the retrovirus-mediated gene transfer, as described previously (Hanawa-Suetsugu et al., 2019). All cell lines were cultured in high glucose DMEM (Thermo Fisher Scientific) supplemented with 10% bovine calf serum (Thermo Fischer Scientific) and 1% penicillin-streptomycin solution (Thermo Fischer Scientific) and stored in an incubator at $37°C$ in 5% CO_2 and humidified conditions. The cells were seeded on coverslips and then imaged with the Lattice light-sheet microscope built in the Mimori-Kiyosue laboratory at RIKEN Center for Biosystems Dynamics Research following the design of the Betzig laboratory (Chen et al., 2014) as described previously (Nishimura et al., 2021).

Note that the concentration of the reconstituted GFP-IRSp53 in the cells is 2–3 times higher than in the normal cells, but it is still within the range if the endogenous level (Mukherjee et al., 2023).

4 Force-binding strength phase diagram

In Fošnarič (2019) the phases of the vesicle with active CMC, were mostly explored as function of temperature and global density of CMC. However, the cell can more easily modify other parameters, such as the strength of the protrusive forces produced by actin polymerization and the binding strength between neighboring CMC. The rate of actin polymerization recruited to the CMC can be controlled by the cell through various proteins (Welch and Mullins, 2002; Carlier and Pantaloni, 2007; Campellone and Welch, 2010). The effective binding strength between the neighboring CMC can similarly depend on the lateral concentration and character of the proteins that form the CMC (Pipathsouk et al., 2021), as well as on the type of lipids between the CMC (Bohinc et al., 2003). The cell can modify these internal parameters spontaneously or in response to external signals.

We scan over the force f and binding strength w parameters plane (Figure 2A), with the other parameters of the model having the following constant values: The bending modulus is taken to be $\kappa = 20K_BT$, which is a typical value for lipid bilayers. The spontaneous curvature of the CMC is taken to be $C_0 = 1\ell_{\min}^{-1}$, representing highly curved objects on the membrane. The CMC density is $\rho = 10\%$, which is sufficient to form the pancake shapes that require a complete circular cluster of CMC along the vesicle rim (Fošnarič et al., 2019). $f \in [0, 1.2]$ and $w \in [0, 4.8]$ were scanned with resolution of 16×16 with three independent simulations per f, w
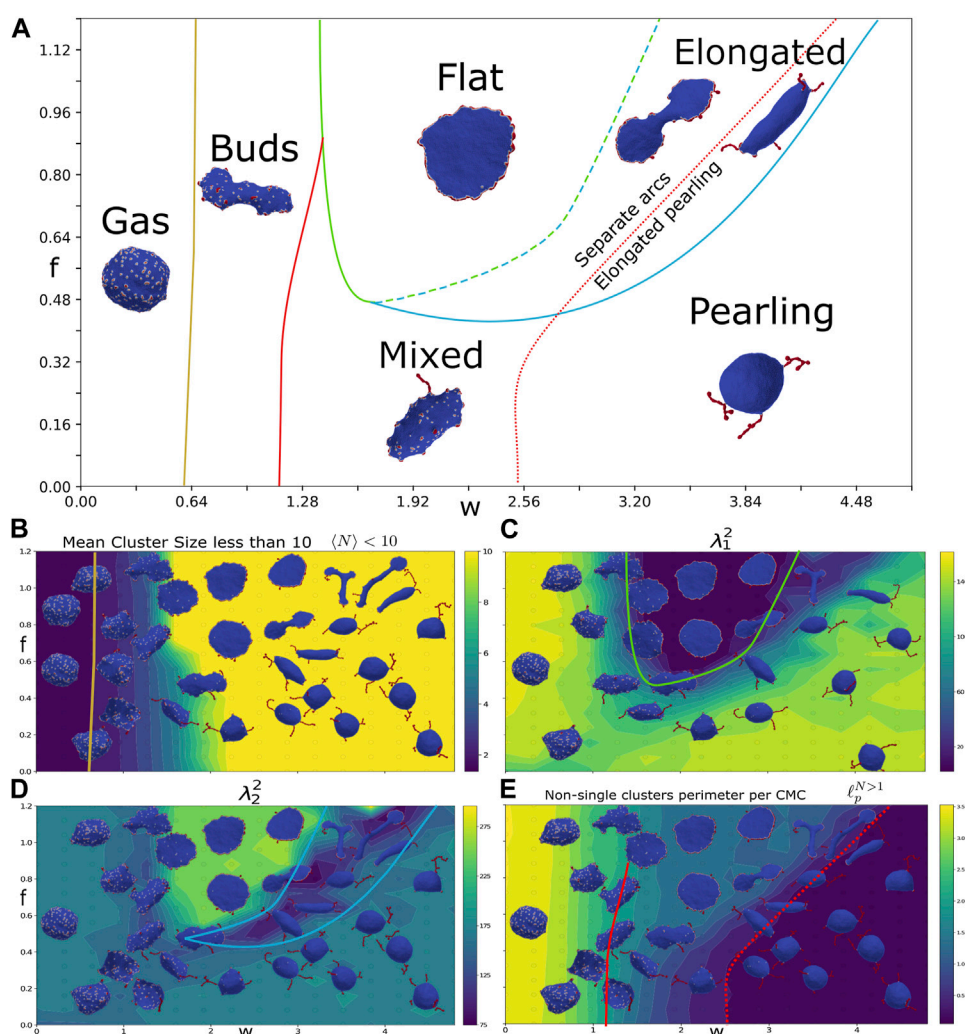
FIGURE 2
Force-binding strength plane. **(A)** Phase diagram as function of f and w, with: κ =20, C_0=1, and ρ =10%. The different phases are indicated by their names, and a typical snapshot of the vesicle after a long simulation is shown. The transition lines between the phases were drawn according to the measures shown in the bottom panels. The gas and buds phase is separated by mean cluster size $\langle N \rangle$ = 1.5 (yellow solid line), as obtained from **(B)**. The green line denotes the boundary of the flat phase, obtained approximately from a contour of the first (small) gyration eigenvalue λ_1^2, which is minimal for flat shapes **(C)**. The light blue line denotes the boundary of the elongated shapes, roughly following a contour of the second (intermediate) gyration eigenvalue λ_2^2 **(D)**. The transition line between the buds and mixed phases is given by a contour of CMC perimeter length ($\bar{\ell}_p$ = 1.875, red solid line), extracted from **(E)**. Finally, the pearling phase transition line (red dotted line) is drawn along the contour of small CMC perimeter length ($\bar{\ell}_p$ = 0.375), from **(E)**. In panels **(B–E)** we plot heatmaps of the following quantities: **(B)** Mean cluster size for clusters smaller than 10, $\langle N \rangle > 10$ **(C)** first (small) gyration eigenvalue λ_1^2, **(D)** second (intermediate) gyration eigenvalue λ_2^2, **(E)** Mean CMC cluster perimeter length (excluding isolated CMC) $\bar{\ell}$.

point in order to get better shape statistics at each point in the phase diagram.

We find that the simulated vesicles can be divided into several distinct phases: gas phase, budded phase, pancake phase, and pearling phase. In addition there are more ambiguous, and possibly transient, elongated and mixed phases (Figure 2A). In order to distinguish between these phases, we use four measures that characterize the vesicle shape and the CMC cluster organization:

- Mean cluster size $\langle N \rangle$
- 1ˢᵗ eigenvalue of the gyration tensor λ_1^2
- 2ⁿᵈ eigenvalue of the gyration tensor λ_2^2

- Length of CMC-bare membrane boundary ℓ_p

The mean cluster size is averaged over all the CMC clusters, each cluster i having a size N_i of vertices

$$\langle N \rangle = \frac{\sum_i N_i}{\sum_i 1} = \frac{N_{\text{vertex}}}{N_{\text{clusters}}}$$

We plot this measure (Figure 2B), extracted after the simulation reaches its steady-state regime, where the measures do not change on average. We see that it allows to clearly distinguish the gas phase, which has small cluster sizes (yellow line in Figure 2A denotes $\langle N \rangle$ = 1.5). However, it is rather poor at separating the condensed phases, which all have large clusters but differ greatly in their

FIGURE 3
Evolution of the MC simulation at four different points **(B−E)** denoted on the phase diagram **(A)** (Figure 2A). **(B)**: f = 0.8, w = 1.6, **(C)**: f = 0.8, w = 2.88, **(D)**: f = 0.8, w = 3.20, and **(E)**: f = 0.4, w = 4.16. The MC time-steps shown in the snapshots are: (i) 10, (ii) 50, and (iii) 200, and the final time-step (299) is shown on the phase diagram **(A)**. At time (i), all simulations are in the budded state. At time (ii), arc and pearling clusters begin to form, favoring arcs for large forces and pearling for large binding strength. At time (iii), the vesicles are close to their final steady-state shapes. The flat simulation **(B)** generates several arcs in stage (ii), which coalesce to form a circular stable rim. The pearling simulation **(E)** generates pearling clusters (ii) which coalesce into a few larger clusters (coarsening). In contrast, the elongated simulations generate both arcs and pearled clusters at the intermediate stage (ii). These arc-like clusters are sufficiently stretch the vesicle, even in **(D)**, to give rise to the final elongated phase.

morphology and cluster organization. This is due to the dependence of this measure on the number of clusters, which gives large weight to small single-vertex clusters. This makes this measure too noisy to distinguish between the other phases, except for the gas phase which mostly contains single-vertex clusters.

We therefore use morphological measures in order to clearly distinguish between the different phases where the CMCs are condensed in large clusters. The morphology of the vesicle is quantified by the eigenvalues of the gyration tensor λ_i^2. The gyration tensor (Theodorou and Suter, 1985) is defined as the average over all the vertices, with respect to the center of mass (similar to the moment of inertia tensor for equal-mass vertices)

$$R_{G\,ij} = \langle r_i r_j \rangle = \frac{1}{N} \sum_{vertices} \begin{pmatrix} x^2 & xy & xz \\ xy & y^2 & yz \\ zx & yz & z^2 \end{pmatrix}$$

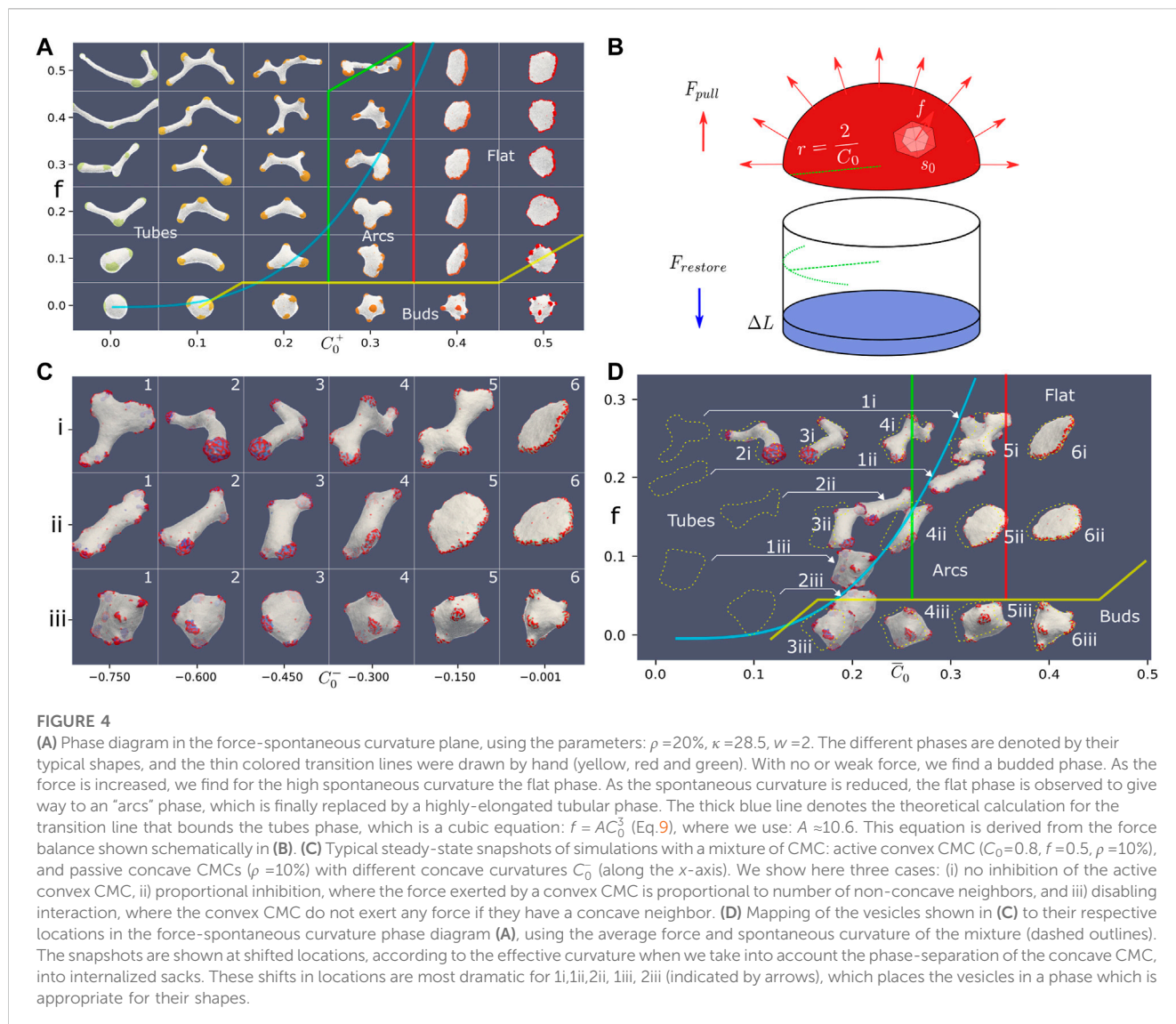This can be visualized by a unique ellipsoid which has the same gyration tensor

$$x^T R_G^{-1} x = \frac{(x \cdot e_1)^2}{\lambda_1^2} + \frac{(x \cdot e_2)^2}{\lambda_2^2} + \frac{(x \cdot e_3)^2}{\lambda_1^2} = 3$$

The eigenvectors e_i of the gyration tensor are the directions of the semi-axes of the equivalent ellipsoid and the eigenvalues are their length squared divided by 3, ordered by their size: $\lambda_1^2 \le \lambda_2^2 \le \lambda_3^2$. The first eigenvalue λ_1 essentially gives how thin is the ellipsoid, and is low for both pancake and highly elongated (linear) shapes. The second eigenvalue λ_2 is large for the pancake shape (as it is roughly equal to the largest eigenvalue $\lambda_2 \sim \lambda_3$), but is minimized for elongated shapes, where it similar to the value of the smallest

eigenvalue, $\lambda_2 \sim \lambda_1$. In Figures 2C,D we plot the eigenvalues λ_1^2, λ_2^2, respectively. We find that the phase of pancake shapes is distinguished by the lowest λ_1^2 (green and dashed green-light blue lines in Figure 2A), indicating its flatness. Note that these two transition lines (from Figures 2C,D) were drawn by hand along the rough contours of these shape measures, since the actual contours were noisy.

We identify a new phase of elongated shapes, which is distinguished by the lowest values of λ_2^2 (between the light blue and dashed green-light blue lines in Figure 2A). These elongated phases are somewhat similar to the "two-arc" phase found in Fošnarič (2019), which appeared when there are not enough CMCs to form a complete circular cluster along the flat vesicle rim. However, here we do have enough CMC to form a complete circular cluster, as shown in the "flat" regime. The origin of the elongated shapes as w increases beyond the "flat" phase is due to the formation of transient or stable pearling clusters. These cluster effectively sequester enough CMC to prevent the formation of the complete circular cluster, leading to two curved regions that collect the CMC and stretch the vesicle due to the active forces. The CMC clusters have the shape of flat arcs near the boundary with the "flat" phase, while closer to the "pearling" phase the clusters are pearled and localized near the curved tips of the vesicle.

While the "core" of the phases distinguished by $\lambda_{1,2}^2$ is clear, the edges are much less sharp, due to lack of statistics, long evolution time, and the fact that intermediate shapes do exist. There is also no obvious normalization: The volume changes greatly, and the area is only approximately conserved. For our $N_{vertex} = 4,502$, the flat phase is found around $\lambda_1^2 < 50$, and the elongated phases is found around $80 < \lambda_2^2 < 150$.

FIGURE 4
(A) Phase diagram in the force-spontaneous curvature plane, using the parameters: ρ =20%, κ =28.5, w =2. The different phases are denoted by their typical shapes, and the thin colored transition lines were drawn by hand (yellow, red and green). With no or weak force, we find a budded phase. As the force is increased, we find for the high spontaneous curvature the flat phase. As the spontaneous curvature is reduced, the flat phase is observed to give way to an "arcs" phase, which is finally replaced by a highly-elongated tubular phase. The thick blue line denotes the theoretical calculation for the transition line that bounds the tubes phase, which is a cubic equation: $f = AC_0^3$ (Eq.9), where we use: $A \approx 10.6$. This equation is derived from the force balance shown schematically in **(B)**. **(C)** Typical steady-state snapshots of simulations with a mixture of CMC: active convex CMC (C_0=0.8, f =0.5, ρ =10%), and passive concave CMCs (ρ =10%) with different concave curvatures C_0^- (along the x-axis). We show here three cases: (i) no inhibition of the active convex CMC, ii) proportional inhibition, where the force exerted by a convex CMC is proportional to number of non-concave neighbors, and iii) disabling interaction, where the convex CMC do not exert any force if they have a concave neighbor. **(D)** Mapping of the vesicles shown in **(C)** to their respective locations in the force-spontaneous curvature phase diagram **(A)**, using the average force and spontaneous curvature of the mixture (dashed outlines). The snapshots are shown at shifted locations, according to the effective curvature when we take into account the phase-separation of the concave CMC, into internalized sacks. These shifts in locations are most dramatic for 1i,1ii,2ii, 1iii, 2iii (indicated by arrows), which places the vesicles in a phase which is appropriate for their shapes.

Finally, we wish to distinguish the phases where the CMCs form pearled clusters. The most outstanding property of the pearled clusters is that they phase-separate between the CMC and the bare membrane, as also predicted within the theory of self-assembly (Fošnarič et al., 2019). We therefore measure the average length of the CMC-bare membrane boundary $\bar{\ell}_p$, per CMC, for all clusters larger than 1 (see Supplementary Material Section S1, Supplementary Figure S1)

$$\bar{\ell}_p = \left\langle \frac{\ell_{pi}}{N_i} \right\rangle_{N_i > 1}$$

The phase with pearling clusters is distinguished by having very low $\bar{\ell}_p < 0.375$ (Figure 2E). We find that this measure identifies the pearled clusters both in the pearling and in the elongated phases (red dotted line in Figure 2A). In addition, a contour of this measure allows us to separate the mixed phase, where the CMC are in both buds and pearled clusters, from the phase that contains only buds (red solid line $\bar{\ell}_p \leq 1.875$ in Figures 2A,E).

Note that we do not know if these phases are necessarily the absolute steady-states of the system in the limit of infinite time. The system might be trapped in a local meta-stable configuration due to dynamical barriers that would require unreasonably long simulations for them to escape. For example, in the regime of low force f and large binding strength w, the global minimum energy configuration should have all the CMC in a single pearled cluster, but during the merging of the pearled clusters into a single cluster they have to overcome bending energy barriers that hinder this process (Golani et al., 2019). In other regimes, such as the elongated phase, we do not know if a stationary steady-state even exists, since the presence of active forces may induce a constantly changing configurations. In the Supplementary Material Section S2 we give a simple analytic calculation that gives reasonably well the transition line between the pearled and flat phases, which are the main stable condensed phases in this phase diagram (Supplementary Figures S2, S3).

The evolution of a handful of chosen simulations are shown in Figure 3, showing flat, elongated-flat, elongated-pearling, and

pearling phases. All the simulations begin in a disordered uniform distribution of the CMC on the spherical vesicle, but in all of them we find that buds form rather quickly (Figure 3Bi–Ei). In the budded phase this configuration simply remains stable and does not evolve significantly. It takes longer time for the larger clusters of the flat rim, arcs and pearls to form. The transition lines separating two different vesicle phases, obtained from our simulations, are not precise, and one can obtain either one of the vesicle shapes close to these lines (Figure 3A).

To conclude, by exploring the $f – w$ phase diagram, we demonstrate the competition between the protein binding which drives the formation of pearled clusters, and the active force that drives the formation of arc-like clusters at the edge of flat protrusion. This competition is highlighted in the new phases of vesicle morphologies that we found, namely the elongated two-arcs and the elongated-pearled phases. The pearling phase appears for large enough values of w, as follows also from the theory of self-assembly (Fošnarič et al., 2019).

5 Force-spontaneous curvature phase diagram

We now proceed to explore the interplay between the active force and the spontaneous curvature of the CMC in determining the morphology of the vesicle. We chose the parameters for a new set of simulations such that we are in the flat phase when the CMC are highly curved: $\rho = 20\%$, $\kappa = 28.5$, $w = 2$. The resulting phase diagram is shown in Figure 4A.

We find several phases: budded phase, flat phase, elongated (arcs) phase and highly-elongated (tubes) phase. Here the boundaries between the different phases were drawn by eye, due to relative sparse scan over the parameters, and the self-evident boundaries (Figure 4A). In this parameter regime, we do not find any pearled phase, with the budded phase remaining stable due to the bending energy barrier that prevents buds merging (note that the bending modulus is larger here), and lower relative w. Similar to the force-binding strength system (Figure 2A), where the budded and pearled phases exist for low active force, we also find that as the active force is increased the budded phase is destabilized to form the flat phase (Figure 4A).

The flat phase is destabilized as the spontaneous curvature decreases due to the following mechanism: as C_0 decreases the thickness of the rim cluster increases, which means that there are not enough CMC to complete a circular cluster around the edge of the flat shape. The morphology then changes into local arc-like clusters that pull the vesicle into elongated shapes. The elongation of these vesicles depends on the magnitude of the active force.

The main feature of this phase diagram is the appearance of the highly-elongated tubular phase, where the entire vesicle is stretch into a several tubes that are pulled by CMC clusters at their tips. We can theoretically estimate the location of the phase transition line, above which a vesicle will become highly-elongated, by comparing the force exerted by the active CMC cluster and the restoring force of the emerging membrane tube due to bending (Figure 4B). A hemispherical CMC cap with radius $r = 2/C_0$ minimizes the bending energy (Eq.1): $E \propto (\frac{1}{r_1} + \frac{1}{r_2} - C_0)^2$, and maximizes the

pulling force (since adding any more CMCs to the cluster, beyond the hemisphere, adds force in the opposite direction). The total pulling force of this hemispherical cluster is given by

$$F_{pull} = f \cdot \underbrace{\frac{1}{2}}_{geometry} \cdot \underbrace{\frac{2\pi (2/C_0)^2}{s_0}}_{\#vertices} \tag{7}$$

where s_0 is the area per vertex, and $2\pi r^2/s_0$ is the number of CMC in the cluster. This hemispherical cap pulls a tube with the same radius from the main vesicle body. Note the extra factor of 1/2 due to the hemispherical shape of the cup, compared to the calculation done for a flat cluster of active proteins in Fošnarič (2019).

Assuming the restoring force is dominated by the bending energy of the membrane tube, it is given by (Eq.1) (Fošnarič et al., 2019)

$$F_{restore} = \frac{\kappa}{2} \frac{2\pi}{(2/C_0)} \tag{8}$$

The highly elongated shape is initiated when the pulling force is greater than this restoring force, so the critical value is given by equating Eqs (7) and (8), which gives

$$f = AC_0^3 \tag{9}$$

where A is a constant determined by the constant parameters of the simulation (bending modulus and average area per vertex). Plotting this simple cubic relation in Figure 4A (blue solid line, where we fit the value of A), shows a good agreement with the observed boundary of the regime of the highly-elongated tubular shapes on the phase diagram. Note however that the shapes of the vesicles at the transition to the tubular phase are not always simple cylindrical tubes with hemispherical clusters at their tips (Figure 4A), as the analytic model assumes (Figure 4B).

To conclude this section, we have shown that active CMC give rise to flat protrusions when they are highly curved. Tubular protrusions can form for weakly curved active CMC, while for highly curved CMC the active force needed to produce such slender protrusions increases extremely fast. In the next sections we explore how slender tubular protrusions can be produced with highly curved active proteins, by either changing the effective curvature of the CMC cluster, or by increasing the effective pulling force of the cluster.

6 Multiple curvature

Real cells have many species of membrane protein of both convex and concave intrinsic curvature. While these membrane proteins have distinct curvatures, the effective curvature of a cluster of CMC may depend on the composition of the cluster, if it contains CMC of different spontaneous curvatures. In order to form clusters of mixed curvatures, we explore vesicles that contain CMC of different curvatures (concave and convex), that bind to each other equally. If the two CMC types bind only to their own kind, they form separate clusters on the vesicle, and their coupling with each other due to curvature alone is rather weak (see Supplementary Material Section S3, Supplementary Figure S4). The convex CMC maintain their activity, as in the previous sections, while the concave CMC is passive.

In Figure 4Ci we show snapshots of the steady-state shapes of the vesicles that contain 10% passive concave CMC, i.e. a CMC species with $C_0^- < 0$ and $f^- = 0$, in addition to convex CMCs ($\rho^+ = 10\%$, $f = 0.5$, and $C_0^+ = 0.8$). Both types of CMC have the same binding strength $w = 2$, which binds both types equally, leading to strong mixing of the two CMC types. For weakly curved concave CMC ($C_0^- = -0.001$) the flat phase remains stable (Figure 4Ci6), driven by the convex active CMC. As the concave CMC become more curved (Figure 4Ci from right to left) the circular cluster at the rim of the flat shape breaks up, and highly elongated shapes appear (Figure 4Ci2,i3).

These shapes can be explained by mapping the vesicles in Figure 4Ci on the phase diagram (Figure 4A). For each simulation, we calculate the average spontaneous curvature of the CMC clusters: $C_{0,eff} = (C_0^+ + C_0^-)/2$, as well as the average pulling force per CMC: $f_{eff} = f/2$. In Figure 4D we plot the typical dashed outline of the vesicles from Figure 4Ci on the phase diagram according to these effective parameters $C_{0,eff}$, f_{eff}. Most vesicles match the shape of the phase to which they are mapped in this way. The only exception is the vesicle with the most concave CMCs (and effective $C_{0,eff} = 0$), which is not in the shape of highly-elongated tubes, as suggested by the calculated average parameters, but fits better the arcs phase. This phenomena is due to the concave CMCs phase-separating into internal "sacks" of concave-enriched clusters (Figure 5Ai), which results in an effective removal of these concave CMC from determining the outer shape of the vesicle. To take this into account, we calculate the effective mean curvature of the CMCs while removing the concave CMC that are contained in the internalized sacks. This is done by including in the calculation of the average curvature only concave CMCs which are connected to at least one convex CMC. Using this revised average spontaneous curvature, we plot the locations of the vesicles on the phase diagram (full snapshots), and find that except for the most curved concave CMC (A1), the locations of the other vesicles is minimally affected. For the case A1, we find that indeed the formations of large sacks of concave CMC, push the vesicle into the arcs regime, compatible with its revised location on the phase diagram. The phase separation of the passive concave CMC into sacks is driven by the minimization of the total bending energy. The highly elongated tubes cost a high bending energy of the bare membrane: in Figure 4Ci2 the average bending energy of the bare membrane is $\sim 25 K_B T$, while in the flatter shapes after the phase separation (Figure 4Ci1) the average bending energy of the bare membrane drops to $\sim 17 K_B T$.

In addition to the overall vesicle shape in the system of mixed curvatures, we are interested in the character of the CMC clusters. We find that concave and convex CMCs create complex mixed clusters with a "coral"- or "sponge"-like texture (Figure 4C and close up in Figure 5Aii). The texture of these clusters seems similar to the membrane ruffles observed in Sitarska et al. (2021) behind the leading edge of motile cells. In this work, the ruffles were attributed to the interaction between concave and convex membrane proteins, that are also involved in the recruitment of the actin polymerization. It was furthermore proposed in Sitarska et al. (2021) that the pattern of ruffles observed in these cells is determined by the interaction between a concave membrane protein that inhibits the actin polymerization, which is recruited by the convex CMC. Motivated by this proposed mechanism, we

explored the resulting shapes of the vesicle and CMC clusters when the concave CMCs inhibit the active force exerted by the convex CMCs. We tested two possibilities: inhibition that is proportional to the number of concave neighbors (Eq.4, Figure 4Cii), and full inhibition with even one concave neighbor (Eq.5, Figure 4Ciii). In both cases we find that the effective force is reduced, and that the resulting shapes correspond very well to their locations on the phase diagram (Figure 4D). The shapes obtained for full inhibition (Figure 4Ciii) are very similar to those for a vesicle with a mixture of passive CMC (see Supplementary Material Section S4, Supplementary Figure S5). Regarding the comparison with the experiments (Sitarska et al., 2021), we conclude from the model that the ruffle texture of the CMC clusters does not crucially depend on the inhibitory interaction between the two CMC types, but rather on their spontaneous curvatures and binding interaction.

Let us now focus on the phase-separated sacks of highly curved concave CMC, which form within the mixed clusters (Figure 5). We observed that the neck that connects the sacks to the outer part of the cluster is much narrower when the convex CMC exert outwards protrusive forces (compare Figure 5Aii,Cii). We quantified the area of the narrowest part of the neck in Figures 5B,D for the active and passive convex CMC, respectively. The necks are naturally narrower for more highly curved concave CMC. The active convex CMC, which push the membrane outwards, exert an effective pressure force that squeezes the neck into a narrower radius. Note that for the narrowest necks, we are clearly at the limit of the spatial resolution of the simulation. We do not allow membrane fission, and therefore can not describe the process of detachment of such sacks as internalized vesicles (Penič et al., 2020), as occurs in cells during endocytosis and macropinocytosis (Kay, 2021).

In Figures 5E,F we show the dynamics of the cluster formation, whereby a patch of passive concave CMC (blues) increase in size, while its rim is populated by active convex CMC (red). In these images the surrounding bare membrane is rendered to be invisible. These simulated dynamics resemble those calculated by another model of macropinocytic cups (Saito and Sawai, 2021), which was based on reaction-diffusion dynamics coupled to active forces.

Finally, in Supplementary Figure S6 we show the steady-state shapes of the vesicles with mixture of CMCs of different curvatures (corresponding to Figures 5Ai,Ci), when adhered to a flat substrate. We find that the concave CMC form sacks that connect to the convex CMC along the rim of the spread vesicle.

7 Force alignment

As we show in Figure 4A, when the highly curved CMC induce a protrusive force that is directed at the outwards normal, we require an extremely large force in order for the highly elongated tubes to form. However, cells initiate slender, tube-like filopodia protrusions using highly curved membrane proteins, such as IRsp53 (Scita et al., 2008; Ahmed et al., 2010; Vaggi et al., 2011; Fox et al., 2022; Tsai et al., 2022; Lee et al., 2023), in agreement with theoretical calculations (Mesarec et al., 2016). Within the slender filopodia in cells, the actin filaments are organized into a cross-linked bundle, which efficiently directs the forces of all the polymerizing actin filaments along the protrusion's axis. The actin nucleators at the tip of the filopodia are different from those at the leading edge of the flat
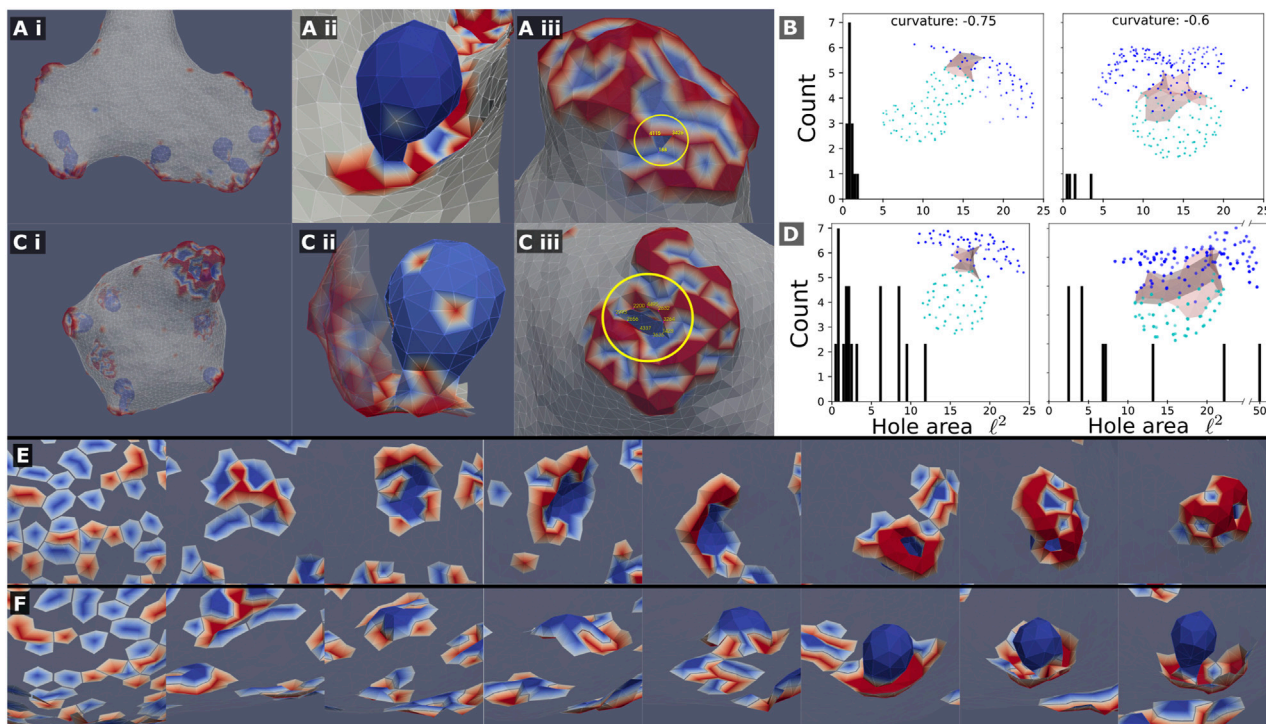
FIGURE 5
Mixed clusters can precipitate internal sacks, which are composed almost entirely of the concave (passive) CMC, when the concave CMCs are highly curved C_0=−0.75,−0.6. This is shown in **(A)** (i,ii),**(C)** (i,ii) for a system with and without active force, respectively. This internal sack is connected to the outside by a thin neck, or "hole", shown in **(A)** (iii) and **(C)** (iii). The cross-sectional area of the hole was measured by computing the area of the polygon made from the hole edge, which was picked by hand (vertices). A histogram of the simulated hole sizes is shown for the system with and without active force respectively **(B−D)**. It is clear that the hole size is smaller in systems with force **(B)**, such that it is in the limit of the simulation resolution. The holes are also larger as the spontaneous curvature of the passive concave CMC is smaller. The insets of **(B−D)** show typical examples of sacks (light blue nodes) connected to the outer part of the cluster (blue nodes) through the neck region (grey shading). **(E)** and **(F)**: Snapshots showing the formation of a sack for the system with active force **(A)**, from the initial random state. In **(E)** we show the cluster viewed from outside of the vesicle (where the bare membrane is rendered invisible), looking down on the patch that forms the sack, while in **(F)** we show the same process viewed from within the vesicle, where we see clearly the final invagination.

lamellipodia (Faix and Rottner, 2006; Faix and Rottner, 2022; Lee et al., 2023), and initiate the growth of parallel actin filaments that form the bundle at the filopodia core. In our model, since we do not explicitly describe the actin filaments organization, we can only describe the effects of the bundling on the forces exerted on the membrane. To simulate this kind of bundling, we add an alignment term of a Vicsek-like interaction (Vicsek and Zafeiris, 2012), which aligns the forces exerted on the membrane by each CMC that is bound in a cluster

$$\hat{f}_i = \frac{\hat{n}_i + s \sum_r \hat{n}_j}{\left|\hat{n}_i + s \sum_r \hat{n}_j\right|} \tag{10}$$

The direction of the active force exerted on each CMC vertex i, $\hat{f}_i$, is a weighted average of the local outwards normal direction ($\hat{n}_i$) and a contribution from all the vertices j within a distance r from the vertex i (and in the same connected cluster), with a weight of s.

In Figure 6A we plot typical steady-state snapshots of the vesicle shape and CMC clusters, as function of the strength and range of the alignment interaction of Eq.10. We observe a rather sharp transition from flat shapes for short-range alignment ($r < 10$) to shapes containing thin tube-like protrusions for long-range alignment. As function of the parameter s we find only weak dependence: at

very small values of s and $r = 10$, we find that the weak alignment is sufficient to increase the net pulling force of the CMC clusters, such that they break the circular rim of the flat shape (Figure 4Biii). The resulting shape, with "paddle"-like protrusions, resembles the "arcs" phase we found in Figure 4 between the flat and tubes phases. At higher values of s this paddles phase changes to tubes, due to the stronger alignment leading to a larger net pulling force.

In the regime of strong alignment interaction strength the vesicle produces thin, finger-like clusters with a small bulbous "head" and an elongated "sleeve" (Figure 6Bii). This shape allows the CMC to satisfy their spontaneous curvature, with a spherical tip that has a radius of $r_{tip} = 2/C_0$, while the sleeve has a thinner radius of $r_{sleeve} = 1/C_0$. Such a cluster configuration is stable due to the alignment of the active forces along the tube axis (perpendicular to the membrane along the sleeve, Figure 6Bii). Once these elongated clusters form, they exert a large pulling force on the remaining membrane, thereby pulling elongated bare-membrane tubes behind them. The membrane tube can have a larger radius than the radius of the tubular CMC cluster, as it balances the pulling force with the restoring force due to bending energy. The alignment of the forces means that the entire CMC cluster pulls along the protrusion axis (Figure 6Bii), exerting a much larger total force
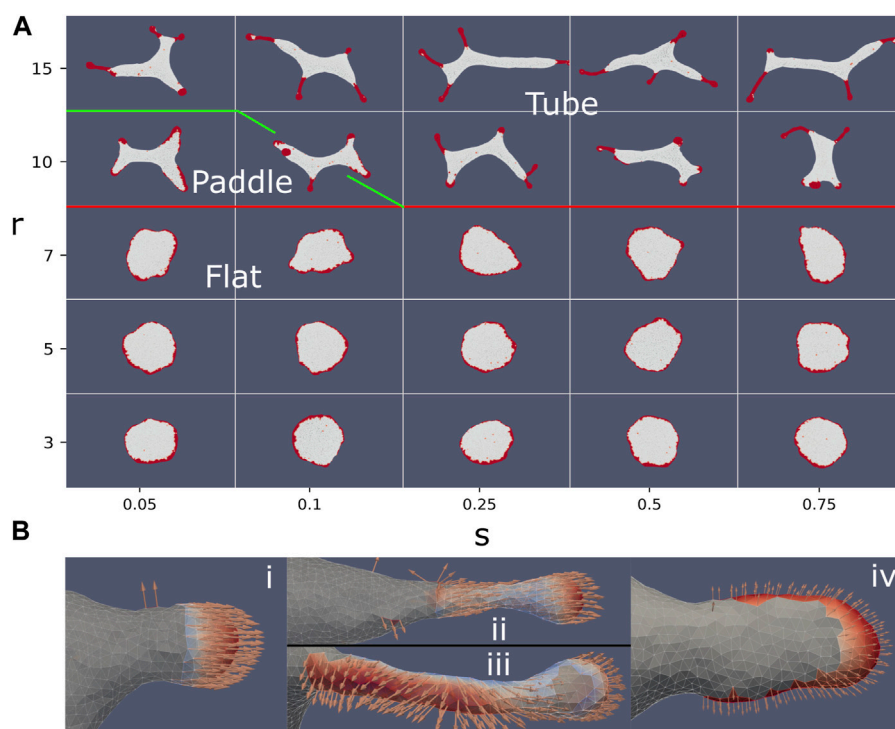
FIGURE 6
(A) Vesicle steady-state shapes as function of the strength (*s*) and range (*r*) of the Vicsek-like alignment interaction (Eq. 10) (ρ =20%, κ =28.5, C_0=0.4, *w* =2, *f* =0.2). Interaction radius smaller than 10 leads to a flat phase. Above an interaction radius of 10, the system transitions from a flat to a tubes phase. In between the flat and elongated tubes phases, we find a phase with "paddle"-like clusters. The tubular phase is characterized by CMC clusters that are mostly finger-like with a bulbous tip and a tubular sleeve, which often stretch a membrane tube behind them. **(B)** Snapshots of CMC clusters, with the active forces indicated by the arrows, and the colormap indicating the dot product of the local force and local outwards normal. In the tubes phase (*s* =0.75, *r* =15) we show in (i) an example of a hemispherical cluster, which is not able to pull an elongated protrusion. In (ii) (top) we show an example of a CMC cluster that contains a tubular sleeve, which increases the net pulling force above the threshold to pull a membrane tube. Note that at the sleeve base the alignment is weak due to the bare membrane boundary. This effect is also shown in (iii) (bottom), where a small patch of bare membrane is trapped between the cluster tip and the sleeve, leading to formation of two different alignment domains within the same cluster. Finally, in (iv) we show an example of the paddle cluster (*s* =0.1, *r* =10), where the weak alignment interaction gives rise to shapes similar to the regular arc-like clusters (Figure 4A), elongated by the non-normal force.

than was possible using purely normal forces at the tip, thereby forming tubes at values of the force per protein that are much lower than predicted by Eq. 9 and Figure 4A. Smaller clusters that only contain the hemispherical tip (such as Figure 6Bi), do not grow tube-like protrusions, even though their net pulling force is larger by up to a factor of 2 compared to normal-force CMC, due to alignment (compare Figure 6Bi to Figure 4B and Eq.7).

In Figure 7A we plot the time progression of a vesicle with aligned-force CMC. We observe that initially localized hemispherical buds form rapidly. These buds then coalesce to form larger clusters that grow into the typical shape of bulbous tip with a thinner tubular part behind it. The size and total force of each of the clusters are plotted as function of time, with each point size indicating the cluster size, and its *y*-axis coordinate giving its total active force, respectively. Note that clusters that contain patches of "trapped" bare membrane undergo large force fluctuations (blue and yellow points, largest two clusters shown on the right of Figure 7A). These fluctuations arise from loss of global alignment over the entire CMC cluster, due to the bare membrane patch that allows the alignment to change, especially between the protrusion tip and the tubular part.

In Figure 7B we compare the finger-like protrusions that form due to highly curved aligned-force CMC, with the tubular shapes that form due to weakly curved normal-force CMC (Figure 4A). The main difference is that the aligned-force protrusions are much more stable compared to the tubes formed by the much smaller clusters of normal-force CMC. The normal-force CMC undergo frequent fission and coalescence events, that correspond to tubes shrinking and regrowing. These differences in dynamics can be seen in the Supplementary Movies S1, S2.

8 Vesicles with both normal and aligned-force CMC, adhered to a flat substrate

In Sadhu et al. (2021) we explored the role of CMC, passive and with normal forces, during the spreading of vesicles on flat adhesive substrates. We found that both passive and the normal-CMC greatly enhance the spreading of the vesicle. In Supplementary Figure S7 we demonstrate that aligned-CMC that produce filopodia-like protrusions alone do not drive
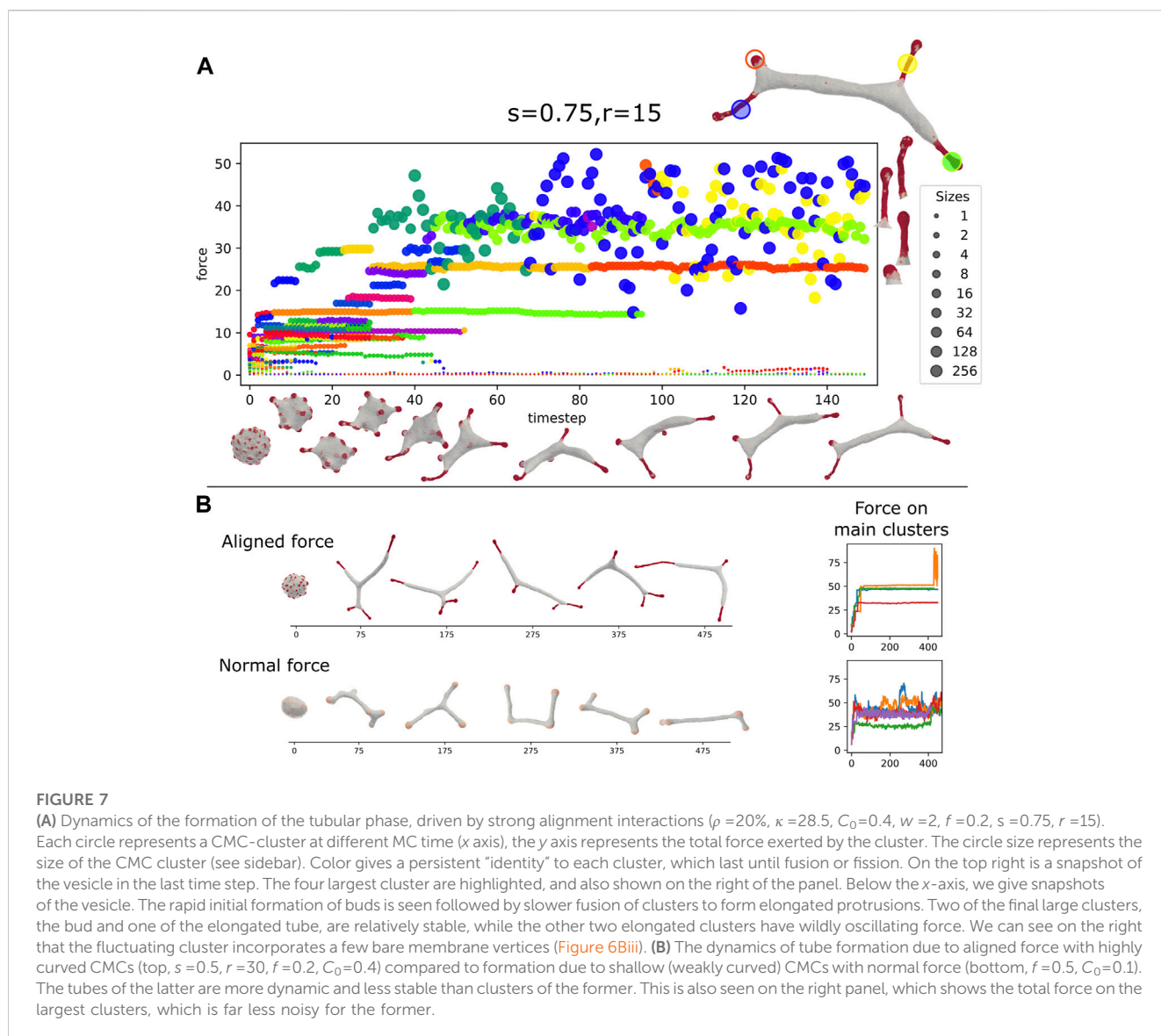
FIGURE 7
(A) Dynamics of the formation of the tubular phase, driven by strong alignment interactions (ρ =20%, κ =28.5, C_0=0.4, w =2, f =0.2, s =0.75, r =15). Each circle represents a CMC-cluster at different MC time (x axis), the y axis represents the total force exerted by the cluster. The circle size represents the size of the CMC cluster (see sidebar). Color gives a persistent "identity" to each cluster, which last until fusion or fission. On the top right is a snapshot of the vesicle in the last time step. The four largest cluster are highlighted, and also shown on the right of the panel. Below the x-axis, we give snapshots of the vesicle. The rapid initial formation of buds is seen followed by slower fusion of clusters to form elongated protrusions. Two of the final large clusters, the bud and one of the elongated tube, are relatively stable, while the other two elongated clusters have wildly oscillating force. We can see on the right that the fluctuating cluster incorporates a few bare membrane vertices (Figure 6Biii). **(B)** The dynamics of tube formation due to aligned force with highly curved CMCs (top, s =0.5, r =30, f =0.2, C_0=0.4) compared to formation due to shallow (weakly curved) CMCs with normal force (bottom, f =0.5, C_0=0.1). The tubes of the latter are more dynamic and less stable than clusters of the former. This is also seen on the right panel, which shows the total force on the largest clusters, which is far less noisy for the former.

efficient spreading, and we therefore study now the spreading driven by mixtures of both aligned and normal CMC.

We simulate a vesicle with a mixture of CMCs (ρ = 5% of each type), both highly curved and convex, one type with normal force and the other with strongly aligned force (r = 15, s = 1). Our initial state of the vesicle is obtained by letting the vesicle spread over a flat adhesive substrate, while it contains only normal-force CMC. Then, at a time where the vesicle is partially spread (time 0 in Figure 8A), we convert randomly half of the CMC to aligned-force behavior. We chose an adhesion strength w_{ad} = 0.25 (Eq.2), which gives a well-spread vesicle when containing only normal-force CMC (Sadhu et al., 2021).

In Figure 8A we show two simulations: one with universal binding between the normal and aligned-force CMCs, and the other with exclusive binding, such that normal-normal and aligned-aligned CMC bind to their own type exclusively. In these examples we see that the rim cluster forms and drives strong spreading of the vesicle, as expected (Sadhu et al., 2021). The aligned-force CMC (labeled in yellow) aggregate to form a single filopodia-like protrusion, which is able to recruit into it also normal-

force CMC (labeled in red). This filopodia is highly dynamic, undergoing periods of attachment to the rim cluster, and to the adhesive substrate, as well as detachments from the substrate. The filopodia is observed to attach and detach from the rim cluster, leading to meandering motion. When the two types bind exclusively, they form segregated clusters along the rim, with the aligned-force clusters protruding slightly more outwards compared to the normal-force clusters. The dynamics of this system can be seen in Supplementary Movie S3.

In Figure 8B we show the evolution of the segregation factor in the simulations, which is defined as

$$S = 2 \cdot \text{Prob}\left(\text{CMC neighbor is of the same type}\right) - 1 \qquad (11)$$

This segregation factor is equal to 0 for well-mixed clusters (where the probability to have a neighbor CMC of the same type is equal to 1/2), and it is equal to 1 for complete phase-separation of the types. In the main panels we give the segregation factor per cluster for the simulations shown in Figure 8A. The insets show the average of 4 independent simulations, which converge to a value of about S = 0.25 for the universal
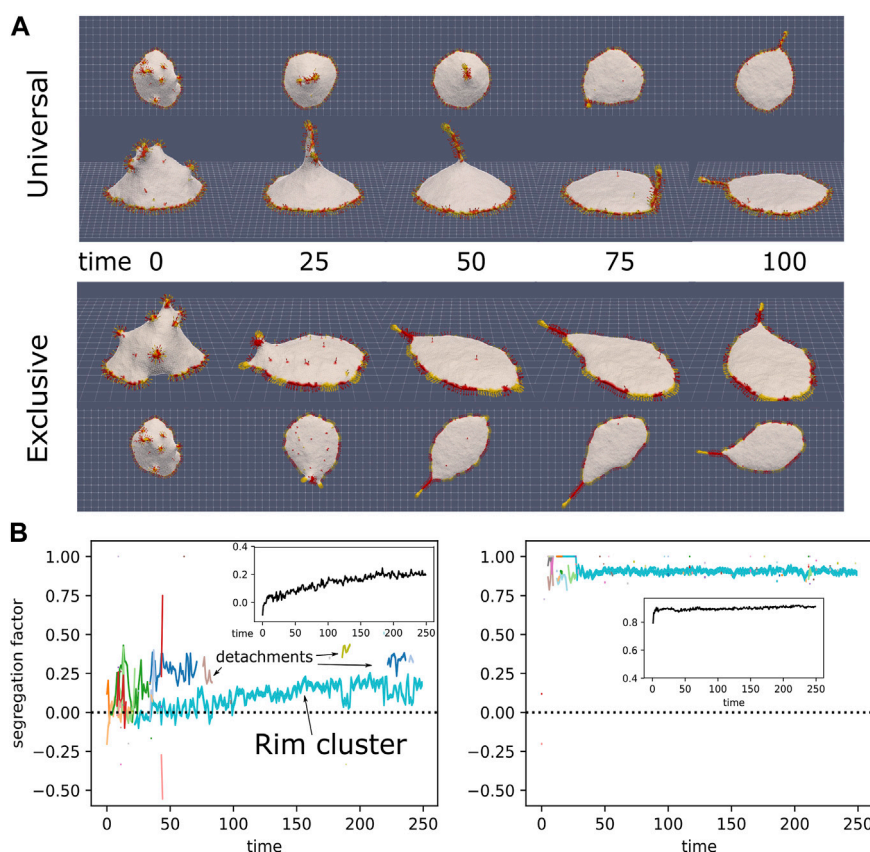
FIGURE 8
(A) Initial progress of simulation with normal-force CMCs (red) and aligned-force CMCs (yellow), in universal binding (top) and type-exclusive binding (bottom), from the side and above (ρ_{align} =10%, ρ_{normal} =10%, κ =28.5, C_0=0.8, w =2, f =0.5, $s_{aligned}$ =1, $r_{aligned}$ =15, w_{ad} =0.25). CMCs in the rim drive the spreading of the vesicle on the surface, while some aligned-force CMCs aggregate into a bulb-and-sleeve cluster which drives the formation of a filopodia-like protrusion. This protrusion can attach to the rim cluster and then adhere to the substrate, while it can also detach from the substrate, and consequently also from the rim cluster. **(B)** Evolution of the segregation factor in the simulations (Eq. 11). The colored lines give the segregation factor for each cluster, with the cluster size indicated by the line thickness. In the inset we give the average of the total segregation factor for 4 independent simulations. In the universal binding simulation we can see the fliopodia-like cluster repeatedly attach and detach from the rim cluster. The rim cluster is mostly mixed for this case, while the protrusion is much more segregated, as its tip is enriched with aligned-force CMCs.

binding and $S = 0.9$ for the exclusive binding. In the universal case, we can see that the segregation is strongest in the filopodia, so the segregation factor for the large rim cluster jumps up or down, when the filopodia protrusion cluster attaches or detaches respectively. The protrusion cluster is more segregated ($S \approx 0.25$), since its tip is enriched with aligned-force CMCs that drive its formation, while the rim cluster is nearly perfectly mixed ($S \approx 0$). For the exclusive binding, the segregation is high both in the filopodia protrusion and in the rim cluster, so it does not change when the filopodia attach or detach from the rim.

Note that along the adhered vesicle rim, the regions of aligned-force CMC protrude slightly more than the normal-force regions (Figure 8A, exclusive). This is enhanced when the normal-force CMC are disabled, so that they do not exert any active force, as shown in Supplementary Figure S8.

9 Comparison with experiments

We can now compare some of our theoretical results to experimental observations, published and new.

9.1 Membrane shapes driven by branched actin polymerization

The active protrusive forces in our model are representative of actin polymerization activity near the cell membrane. When the actin polymerization is nucleated by proteins that induce branched actin networks (such as WASP, WAVE (Small et al., 2002; Takenawa and Suetsugu, 2007; Rottner and Schaks, 2019)), it is more natural to describe the force as a local pressure on the membrane, which therefore acts towards the outwards normal.

The variety of shapes we obtained in our model (Figures 2, 3), range from flat lamellipodia-like shapes, to cylindrical filopodia, to pearling-like protrusions. Some of these new elongated shapes can be compared with elongated global cell shapes, observed in living cells (Suetsugu et al., 2006). Note that the thickness of the flat vesicle in our model is close to $1/C_0$. However, note that our CMC do not necessarily correspond to single membrane proteins, but rather to larger complexes of proteins which can therefore have an effective radius of curvature that is of order of 10s of nanometers, which agree with the observed thickness of lamellipodia and sheet-like ruffles.

9.2 Membrane shapes driven by bundled actin polymerization

The introduction of alignment in the forces exerted by the CMC represents in our model the case of proteins that nucleate parallel actin bundles, such as VASP and Formins (Faix and Rottner, 2006; Vaggi et al., 2011; Tsai et al., 2022). Our model has demonstrated previously that curved proteins that apply normal forces, induce the formation of flattened, lamellipodia-like protrusions (Fošnarič et al., 2019; Sadhu et al., 2021). Here we show that curved proteins that induce polymerization of bundled actin (aligned-force in our model), naturally give rise to filopodia-like protrusions (Figures 6, 7). This result fits the observation of highly curved convex-shaped proteins such as IRSp53 in both the leading edge of lamellipodia (Pipathsouk et al., 2021; Pawluchin and Galic, 2022) and in filopodia (Mattila and Lappalainen, 2008; Mancinelli et al., 2021), where the actin organization is very different due to the different type of actin nucleators (Small et al., 2002; Krause and Gautreau, 2014). Note that the combination of convex curvature, and nucleators of bundled actin, can form filopodia even without the explicit presence of I-BAR proteins (such as IRSp53) (Kühn et al., 2015; Pokrant et al., 2023).

The forces exerted by the aligned-CMC in our model are not always perfectly along the axis of the protrusion, as shown in Figure 6Bii,iii. We are not aware of any available direct measurements of the forces exerted by the actin filaments on the membrane at sub-filopodia resolution. However, it was found by EM studies that the actin filaments inside filopodia are not all perfectly aligned along the main bundle axis (Medalia et al., 2007). Intricate details of the bundle shape (Li et al., 2022), are of course beyond the scope of our model.

Note that protrusions of similar shapes to our aligned-force protrusions, which have a bulbous tip and a slender neck (Figures 6, 7), were theoretically predicted to form by anisotropic CMC, even without force (Bobrovska et al., 2013). Similar thin tubes with bulbous tips are observed in cellular nanotubes (Schara et al., 2009) and in filopodia (Miihkinen et al., 2021; Li et al., 2022). Since many curved proteins, such as IRSp53 are anisotropic in their intrinsic shape, it will be interesting to extend our work in the future to include such anisotropy.

Finally, our simulations of an adhered vesicle (Figure 8) indicate that the filopodia protrusions can undergo attachment and detachment from the substrate, resembling such motion observed in experiments (Lee et al., 2023). In addition, when we mixed the aligned-force and normal-force CMC with exclusive binding between them, we obtained their segregated organization along the rim of the adhered vesicle. This is reminiscent of the observations of segregated regions of bundled actin and branched actin nucleators along the rim of cellular protrusions extending on adhered substrates (Cohan et al., 2001; Damiano-Guercio et al., 2020; Faix and Rottner, 2022; Kage et al., 2022). As in the experiments, the clusters of aligned-force CMC along the rim slightly protrude, as they exert a higher local force on the membrane rim, compared to the normal-force CMC. These small protrusions have been termed "spikes" and "microspikes" along the edge of lamellipodia in cells (Koestler et al., 2008; Damiano-Guercio et al., 2020; Pokrant et al., 2023).

In Figure 9 we show images illustrating the dynamics of filopodia in cells, using lattice light-sheet microscopy, which is capable of the high spatial and temporal resolution necessary to view the dynamics of thin filopodia (Mimori-Kiyosue, 2023). The curved membrane protein IRSp53 is fluorescently labeled in green (GFP-IRSp53), while the actin filaments are labeled in red (mCherry-lifeact). We observe in the experiments several features that are captured by the theoretical model: The filopodia are highly dynamic, both at the cell rim and along its dorsal surface (Figures 9A–D), as we also see in the model (Figure 8). The filopodia in the experiments migrate on the cell surface, merge with other filopodia, and undergo attachments and detachments from the surface (see Supplementary Movies S5–S8), as we also see in the simulations (Supplementary Movies S3, S4). Our assumption in the model of uniform adhesion along the membrane, and along the filopodia, agrees with some observations (Miihkinen et al., 2021; Tu et al., 2022), and we can add more complex adhesion models in the future if needed. Note that in the cells we observe an additional retraction motion that is driven by myosin-II contractile forces, which we do not have in our current model.

The highly curved IRSp53 is observed to aggregate strongly at the tips of the filopodia, while along the lower parts of the protrusion its aggregation is more fragmented (Figures 9E,F). This fits with the shapes that we obtained in the model (Figures 6B, 8A). Furthermore, our simulations of mixtures of aligned-force and normal-force CMC indicate that while the aligned-force CMC are essential for forming the filopodia protrusions and occupy its tip region, there can be significant amount of normal-force CMC along the lower part of the filpodia. Since the normal-force CMC correspond to branched-actin nucleators, this result suggests that along the lower part of filopodia we may expect to find proteins such as WAVE, which are usually associated with the leading edge of the lamellipodia. This prediction is supported by some experimental observations of WAVE proteins (Nozumi et al., 2003), Arp2/3 complexes (Johnston et al., 2008), and small lamellipodia-like protrusions, along filopodia shafts (Lebrand et al., 2004).

9.3 Membrane shapes driven by mixtures of passive concave and active convex CMC

Our mixtures of CMC of opposite curvatures (Figures 4C, 5) gives rise to membrane shapes that resemble in their texture the ruffles observed in cells (Sitarska et al., 2021). In addition, we find that when the passive concave component is highly curved, we observe a phase separation within the CMC clusters, whereby the concave CMC forms an internalized spherical invagination. These invaginations are then squeezed at their base by the active forces induced by the convex CMC, and the calculated membrane shape dynamics resembles the observed process of actin-dependent endocytosis (Doherty and McMahon, 2009; Mooren et al., 2012; Moreno-Layseca et al., 2021; Kaplan et al., 2022) and macropinocytosis (Kay, 2021; Mylvaganam et al., 2021; Sønder et al., 2021; Lutton et al., 2022).

Note that there is some experimental evidence that the internalized membrane, corresponding to our concave CMC region, do indeed contain concave membrane components, such as BAR proteins (Baranov et al., 2019). In addition, there are examples where the internalized region contains membrane components that interact with the convex proteins that recruit actin and form the squeezing at the narrow neck. In Moreno-Layseca et al. (2021) the internalized activated integrins and
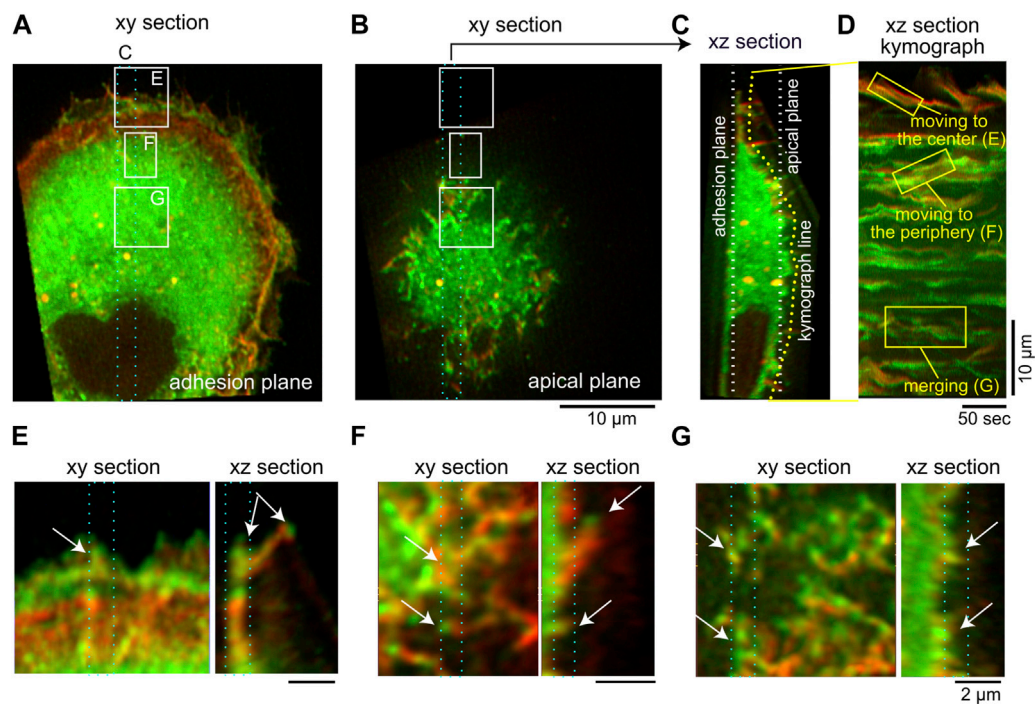
FIGURE 9
Movements of IRSp53-localized cellular protrusions visualized by lattice light-sheet microscopy. **(A,B)** The adhesion **(A)** and apical **(B)** plane section of the three-dimensional images of an IRSp53-knockout U251 glioblastoma cell expressing GFP-IRSp53 (green) and mCherry-lifeact (red). In **(A)** and **(B)**, the region for the ~ 2 μm thick xz section projection is indicated by the cyan dotted rectangle. **(C)** The xz section of the region of **(A)**. The white lines indicate the plane in **(A,B)**. The yellow line, which was set in the proximity of the surface plane of the cell, indicates the line for the kymograph. **(D)** The kymograph of the cell surface as indicated in the yellow line in **(C)**, along with the annotation of the representative motion of the IRSp53. **(E,F)** The xy and xz sections at the regions that are marked in **(A,B)**, from the periphery **(E)**, the middle **(F)**, and the center **(G)**. The plane parallel to the plasma membrane was sectioned and the regions that were projected xy and xz sections each others were marked in cyan dotted rectangles. Arrows indicate the protrusions. The scale bar, 10 μm **(A–D)**, 2 μm **(E−G)**, and 50 s **(D)**. See also Supplementary Movies S5–S8.

associated proteins, bind to the actin which is nucleated at the neck, recruited there by IRSp53 (convex) proteins. In our model we show that such a direct interaction is necessary for robust formation of the internalized sacks with the recruited convex proteins at the neck.

10 Discussion

In this study we greatly extend our theoretical understanding of the space of membrane shapes that are produced by curved membrane protein complexes (CMC) that exert active protrusive forces on the membrane (Drab et al., 2023). We started by mapping the phases as function of the magnitude of the active force and attractive nearest-neighbor interaction strength of CMCs (Figure 2A), demonstrating the competition between these two terms: systems dominated by the binding interactions tend to have the equilibrium (pearled) shapes of the CMC clusters. The active forces tend to break-up the pearled clusters, and induce the formation of either elongated or flat pancake-like membrane shapes.

Similarly we exposed the phase diagram in terms of the active force and the CMC spontaneous curvature (Figure 4A), whereby highly curved CMC induce flattened vesicle shapes, while less curved CMC induce elongated tubular shapes. Note that in these studies the protrusive force applied by each CMC is towards the local outwards normal.

Based on these results we further explored systems where highly curved active CMC could induce tubular protrusions. We tested two possible scenarios: In the first one, the effective curvature of the CMC cluster is reduced by mixing two types of CMC of opposite curvatures, such that a tubular protrusion forms with a rather flat CMC cluster at its tip (Figures 4C,D). In the second, the net protrusive force of the CMC cluster is increased by introducing an alignment interaction that tends to align the forces exerted by CMC that are bound within the same cluster (Figure 6). This alignment is found to stabilize long tubular CMC clusters, since the aligned active forces act along the tube axis and do not act to expand the tube, unlike the case of normal protrusive forces.

We found that mixtures of CMC of opposite curvatures, specifically passive concave and active convex, lead to formation of clusters with complex textures that resemble ruffles on cell membranes (Figures 4C, Figures 5). In addition, we found in these systems the formation of internalized invaginations, where the convex active CMC form a narrow neck, resembling endocytosis and macropinocytosis in cells. revi.

Note that there are many additional components of the cell membrane which we do not explicitly describe in our model. For example, the cortical actin layer that is adsorbed to the membrane can effectively rigidify the membrane and resist its bending (Xia et al., 2019; Svitkina, 2020). We could in the future take this effect into account by varying the bending modulus of the membrane (Eqs. 1, 2), and making

it spatially non-uniform. In addition, future studies could explore the effects of volume conservation and including an osmotic pressure that inflates the vesicle. Similarly, contractile forces, that are produced due to myosin-II activity, could be added to the model.

To conclude, the results presented in this work expand out theoretical understanding of membrane shapes and dynamics driven by intrinsic (spontaneous) curvature of membrane components and cytoskeletal active forces. Some of these shapes resemble observed membrane dynamics in living cells, suggesting that this coupling between curved membrane proteins and cytoskeleton forces gives rise to these biological phenomena. Many of the features that we found, such as the ruffles and the internalized invaginations by mixing CMC of different curvatures, remain to be further explored in future theoretical studies. In addition, future studies will explore the dynamics of the membranes when the CMC have anisotropic spontaneous curvature, and also in the presence of contractile forces.

Data availability statement

The datasets presented in this study can be found in online repositories. The names of the repository/repositories and accession number(s) can be found below: Code repository https://github.com/ yoavrv/cluster-trisurf. Box repository for paper, movies, and material to recreate simulations https://weizmann.app.box.com/s/ 5z6aexxk1lmne0b29sf25o451unnj85x.

Author contributions

YR and NG developed the theoretical model; SP and AI developed the software; YR and NG conceived, designed and implemented the analysis of the model, and prepared the manuscript. YK and SS cultured and imaged the cells. The manuscript was edited by all the authors.

Funding

Acknowledgments

Conflict of interest

The authors declare that the research was conducted in the absence of any commercial or financial relationships that could be construed as a potential conflict of interest.

Publisher's note

All claims expressed in this article are solely those of the authors and do not necessarily represent those of their affiliated organizations, or those of the publisher, the editors and the reviewers. Any product that may be evaluated in this article, or claim that may be made by its manufacturer, is not guaranteed or endorsed by the publisher.

Supplementary material

The Supplementary Material for this article can be found online at: https://www.frontiersin.org/articles/10.3389/fmolb.2023.1153420/ full#supplementary-material

References

Ahmed, S., Goh, W. I., and Bu, W. (2010). I-bar domains, irsp53 and filopodium formation. *Seminars Cell & Dev. Biol.* 21, 350–356. doi:10.1016/j.semcdb.2009.11.008

Baranov, M. V., Olea, R. A., and van den Bogaart, G. (2019). Chasing uptake: Super-resolution microscopy in endocytosis and phagocytosis. *Trends Cell Biol.* 29, 727–739. doi:10.1016/j.tcb.2019.05.006

Begemann, I., Saha, T., Lamparter, L., Rathmann, I., Grill, D., Golbach, L., et al. (2019). Mechanochemical self-organization determines search pattern in migratory cells. *Nat. Phys.* 15, 848–857. doi:10.1038/s41567-019-0505-9

Bobrovska, N., Góźdź, W., Kralj-Iglič, V., and Iglič, A. (2013). On the role of anisotropy of membrane components in formation and stabilization of tubular structures in multicomponent membranes. *PloS One* 8, e73941. doi:10.1371/journal.pone.0073941

Bohinc, K., Kralj-Iglič, V., and May, S. (2003). Interaction between two cylindrical inclusions in a symmetric lipid bilayer. *J. Chem. Phys.* 119, 7435–7444. doi:10.1063/1.1607305

Campellone, K. G., and Welch, M. D. (2010). A nucleator arms race: Cellular control of actin assembly. *Nat. Rev. Mol. Cell Biol.* 11, 237–251. doi:10.1038/nrm2867

Carlier, M. F., and Pantaloni, D. (2007). Control of actin assembly dynamics in cell motility. *J. Biol. Chem.* 282, 23005–23009. doi:10.1074/jbc.R700020200

Chen, B. C., Legant, W. R., Wang, K., Shao, L., Milkie, D. E., Davidson, M. W., et al. (2014). Lattice light-sheet microscopy: Imaging molecules to embryos at high spatiotemporal resolution. *Science* 346, 1257998. doi:10.1126/science.1257998

Cohan, C. S., Welnhofer, E. A., Zhao, L., Matsumura, F., and Yamashiro, S. (2001). Role of the actin bundling protein fascin in growth cone morphogenesis: Localization in filopodia and lamellipodia. *Cell Motil. Cytoskelet.* 48, 109–120. doi:10.1002/1097-0169(200102)48:2<109::AID-CM1002>3.0.CO;2-G

Damiano-Guercio, J., Kurzawa, L., Mueller, J., Dimchev, G., Schaks, M., Nemethova, M., et al. (2020). Loss of ena/vasp interferes with lamellipodium architecture, motility and integrin-dependent adhesion. *eLife* 9, e55351. doi:10.7554/eLife.55351

Doherty, G. J., and McMahon, H. T. (2009). Mechanisms of endocytosis. *Annu. Rev. Biochem.* 78, 857–902. doi:10.1146/annurev.biochem.78.081307.110540

Drab, M., Sadhu, R. K., Ravid, Y., Iglič, A., Kralj-Iglič, V., and Gov, N. S. (2023). Modeling cellular shape changes in the presence of curved membrane proteins and

active cytoskeletal forces. *Plasma Membr. Shap.* 2023, 415–429. doi:10.1016/b978-0-323-89911-6.00002-9

Faix, J., and Rottner, K. (2022). Ena/vasp proteins in cell edge protrusion, migration and adhesion. *J. Cell Sci.* 135, jcs259226. doi:10.1242/jcs.259226

Faix, J., and Rottner, K. (2006). The making of filopodia. *Curr. Opin. Cell Biol.* 18, 18–25. doi:10.1016/j.ceb.2005.11.002

Fošnarič, M., Penič, S., Iglič, A., Kralj-Iglič, V., Drab, M., and Gov, N. S. (2019). Theoretical study of vesicle shapes driven by coupling curved proteins and active cytoskeletal forces. *Soft Matter* 15, 5319–5330. doi:10.1039/c8sm02356e

Fox, S., Tran, A., Trinkle-Mulcahy, L., and Copeland, J. W. (2022). Cooperative assembly of filopodia by the formin fmnl2 and i-bar domain protein irtks. *J. Biol. Chem.* 298, 102512. doi:10.1016/j.jbc.2022.102512

Frey, F., and Idema, T. (2021). More than just a barrier: Using physical models to couple membrane shape to cell function. *Soft Matter* 17, 3533–3549. doi:10.1039/d0sm01758b

Golani, G., Ariotti, N., Parton, R. G., and Kozlov, M. M. (2019). Membrane curvature and tension control the formation and collapse of caveolar superstructures. *Dev. Cell* 48, 523–538. doi:10.1016/j.devcel.2018.12.005

Gov, N. (2018). Guided by curvature: Shaping cells by coupling curved membrane proteins and cytoskeletal forces. *Philosophical Trans. R. Soc. B Biol. Sci.* 373, 20170115. doi:10.1098/rstb.2017.0115

Gov, N. S., Kralj-Iglič, V., Sadhu, R. K., Mesarec, L., and Iglič, A. (2023). Physical principles of cellular membrane shapes. *Plasma Membr. Shap.* 2023, 393–413. doi:10.1016/B978-0-323-89911-6.00025-X

Graziano, B. R., Town, J. P., Sitarska, E., Nagy, T. L., Fošnarič, M., Penič, S., et al. (2019). Cell confinement reveals a branched-actin independent circuit for neutrophil polarity. *PLoS Biol.* 17, e3000457. doi:10.1371/journal.pbio.3000457

Hanawa-Suetsugu, K., Itoh, Y., Ab Fatah, M., Nishimura, T., Takemura, K., Takeshita, K., et al. (2019). Phagocytosis is mediated by two-dimensional assemblies of the f-bar protein gas7. *Nat. Commun.* 10, 4763. doi:10.1038/s41467-019-12738-w

Johnston, S. A., Bramble, J. P., Yeung, C. L., Mendes, P. M., and Machesky, L. M. (2008). Arp2/3 complex activity in filopodia of spreading cells. *BMC Cell Biol.* 9, 65–17. doi:10.1186/1471-2121-9-65

Kage, F., Döring, H., Mietkowska, M., Schaks, M., Grüner, F., Stahnke, S., et al. (2022). Lamellipodia-like actin networks in cells lacking wave regulatory complex. *J. Cell Sci.* 135, jcs260364. doi:10.1242/jcs.260364

Kaplan, C., Kenny, S. J., Chen, X., Schöneberg, J., Sitarska, E., Diz-Muñoz, A., et al. (2022). Load adaptation by endocytic actin networks. *Mol. Biol. Cell* 33, ar50. doi:10.1091/mbc.E21-11-0589

Kay, R. R. (2021). Macropinocytosis: Biology and mechanisms. *Cells Dev.* 168, 203713. doi:10.1016/j.cdev.2021.203713

Koestler, S. A., Auinger, S., Vinzenz, M., Rottner, K., and Small, J. V. (2008). Differentially oriented populations of actin filaments generated in lamellipodia collaborate in pushing and pausing at the cell front. *Nat. Cell Biol.* 10, 306–313. doi:10.1038/ncb1692

Krause, M., and Gautreau, A. (2014). Steering cell migration: Lamellipodium dynamics and the regulation of directional persistence. *Nat. Rev. Mol. Cell Biol.* 15, 577–590. doi:10.1038/nrm3861

Kühn, S., Erdmann, C., Kage, F., Block, J., Schwenkmezger, L., Steffen, A., et al. (2015). The structure of fmnl2–cdc42 yields insights into the mechanism of lamellipodia and filopodia formation. *Nat. Commun.* 6, 7088. doi:10.1038/ncomms8088

Lebrand, C., Dent, E. W., Strasser, G. A., Lanier, L. M., Krause, M., Svitkina, T. M., et al. (2004). Critical role of ena/vasp proteins for filopodia formation in neurons and in function downstream of netrin-1. *Neuron* 42, 37–49. doi:10.1016/s0896-6273(04)00108-4

Lee, S. Y., Fujioka, T., Osuga, M., Nishimura, T., and Suetsugu, S. (2023). *Lamellipodia and filopodia*. Plasma membrane shaping. Elsevier, 245–263.

Li, W., Chung, W. L., Kozlov, M. M., Medalia, O., Geiger, B., and Bershadsky, A. (2022). *Chiral growth of adherent filopodia*. bioRxiv.

Lutton, J., Paschke, P., Munn, C., King, J. S., Kay, R., Bretschneider, T., et al. (2022). *The formation and closure of macropinocytic cups in a model system*. bioRxiv.

Mancinelli, G., Lamparter, L., Nosov, G., Saha, T., Pawluchin, A., Kurre, R., et al. (2021). Dendrite tapering actuates a self-organizing signaling circuit for stochastic filopodia initiation in neurons. *Proc. Natl. Acad. Sci.* 118, e2106921118. doi:10.1073/pnas.2106921118

Mashiko, D., Fujihara, Y., Satouh, Y., Miyata, H., Isotani, A., and Ikawa, M. (2013). Generation of mutant mice by pronuclear injection of circular plasmid expressing cas9 and single guided rna. *Sci. Rep.* 3, 3355–3356. doi:10.1038/srep03355

Mattila, P. K., and Lappalainen, P. (2008). Filopodia: Molecular architecture and cellular functions. *Nat. Rev. Mol. Cell Biol.* 9, 446–454. doi:10.1038/nrm2406

McMahon, H. T., and Boucrot, E. (2015). Membrane curvature at a glance. *J. Cell Sci.* 128, 1065–1070. doi:10.1242/jcs.114454

Medalia, O., Beck, M., Ecke, M., Weber, I., Neujahr, R., Baumeister, W., et al. (2007). Organization of actin networks in intact filopodia. *Curr. Biol.* 17, 79–84. doi:10.1016/j.cub.2006.11.022

Mellor, H. (2010). The role of formins in filopodia formation. *Biochimica Biophysica Acta (BBA)-Molecular Cell Res.* 1803, 191–200. doi:10.1016/j.bbamcr.2008.12.018

Mesarec, L., Góźdź, W., Iglič, V. K., Kralj, S., and Iglič, A. (2016). Closed membrane shapes with attached bar domains subject to external force of actin filaments. *Colloids Surfaces B Biointerfaces* 141, 132–140. doi:10.1016/j.colsurfb.2016.01.010

Miihkinen, M., Grönloh, M. L., Popović, A., Vihinen, H., Jokitalo, E., Goult, B. T., et al. (2021). Myosin-x and talin modulate integrin activity at filopodia tips. *Cell Rep.* 36, 109716. doi:10.1016/j.celrep.2021.109716

Mimori-Kiyosue, Y. (2023). Imaging three-dimensional dynamics of plasma membrane structures using ultrathin plane illumination microscopy. *Plasma Membr. Shap.* 2023, 357–374. doi:10.1016/B978-0-323-89911-6.00004-2

Mooren, O. L., Galletta, B. J., and Cooper, J. A. (2012). Roles for actin assembly in endocytosis. *Annu. Rev. Biochem.* 81, 661–686. doi:10.1146/annurev-biochem-060910-094416

Moreno-Layseca, P., Jäntti, N. Z., Godbole, R., Sommer, C., Jacquemet, G., Al-Akhrass, H., et al. (2021). Cargo-specific recruitment in clathrin-and dynamin-independent endocytosis. *Nat. Cell Biol.* 23, 1073–1084. doi:10.1038/s41556-021-00767-x

Mukherjee, A., Ron, J. E., Hu, H. T., Nishimura, T., Hanawa-Suetsugu, K., Behkam, B., et al. (2023). Actin filaments couple the protrusive tips to the nucleus through the i-bar domain protein irsp53 during the migration of cells on 1d fibers. *Adv. Sci.* 10, 2207368. doi:10.1002/advs.202207368

Mylvaganam, S., Freeman, S. A., and Grinstein, S. (2021). The cytoskeleton in phagocytosis and macropinocytosis. *Curr. Biol.* 31, R619–R632. doi:10.1016/j.cub.2021.01.036

Nishimura, T., Oyama, T., Hu, H. T., Fujioka, T., Hanawa-Suetsugu, K., Ikeda, K., et al. (2021). Filopodium-derived vesicles produced by mim enhance the migration of recipient cells. *Dev. Cell* 56, 842–859.e8. doi:10.1016/j.devcel.2021.02.029

Nozumi, M., Nakagawa, H., Miki, H., Takenawa, T., and Miyamoto, S. (2003). Differential localization of wave isoforms in filopodia and lamellipodia of the neuronal growth cone. *J. Cell Sci.* 116, 239–246. doi:10.1242/jcs.00233

Pawluchin, A., and Galic, M. (2022). Moving through a changing world: Single cell migration in 2d vs. 3d. *Front. Cell Dev. Biol.* 10, 1080995. doi:10.3389/fcell.2022.1080995

Penič, S., Mesarec, L., Fošnarič, M., Mrówczyńska, L., Hägerstrand, H., Kralj-Iglič, V., et al. (2020). Budding and fission of membrane vesicles: A mini review. *Front. Phys.* 8, 342. doi:10.3389/fphy.2020.00342

Pipathsouk, A., Brunetti, R. M., Town, J. P., Graziano, B. R., Breuer, A., Pellett, P. A., et al. (2021). The wave complex associates with sites of saddle membrane curvature. *J. Cell Biol.* 220, e202003086. doi:10.1083/jcb.202003086

Pokrant, T., Hein, J. I., Körber, S., Disanza, A., Pich, A., Scita, G., et al. (2023). Ena/vasp clustering at microspike tips involves lamellipodin but not i-bar proteins, and absolutely requires unconventional myosin-x. *Proc. Natl. Acad. Sci.* 120, e2217437120. doi:10.1073/pnas.2217437120

Rottner, K., and Schaks, M. (2019). Assembling actin filaments for protrusion. *Curr. Opin. Cell Biol.* 56, 53–63. doi:10.1016/j.ceb.2018.09.004

Sadhu, R. K., Penič, S., Iglič, A., and Gov, N. S. (2021). Modelling cellular spreading and emergence of motility in the presence of curved membrane proteins and active cytoskeleton forces. *Eur. Phys. J. Plus* 136, 495. doi:10.1140/epjp/s13360-021-01433-9

Saito, N., and Sawai, S. (2021). Three-dimensional morphodynamic simulations of macropinocytic cups. *Iscience* 24, 103087. doi:10.1016/j.isci.2021.103087

Schara, K., Janša, V., Šuštar, V., Dolinar, D., Pavlič, J. I., Lokar, M., et al. (2009). Mechanisms for the formation of membranous nanostructures in cell-to-cell communication. *Cell. Mol. Biol. Lett.* 14, 636–656. doi:10.2478/s11658-009-0018-0

Scita, G., Confalonieri, S., Lappalainen, P., and Suetsugu, S. (2008). Irsp53: Crossing the road of membrane and actin dynamics in the formation of membrane protrusions. *Trends Cell Biol.* 18, 52–60. doi:10.1016/j.tcb.2007.12.002

Simunovic, M., Voth, G. A., Callan-Jones, A., and Bassereau, P. (2015). When physics takes over: BAR proteins and membrane curvature. *Trends Cell Biol.* 25, 780–792. doi:10.1016/j.tcb.2015.09.005

Sitarska, E., Almeida, S. D., Beckwith, M. S., Stopp, J., Schwab, Y., Sixt, M., et al. (2021). *Sensing their plasma membrane curvature allows migrating cells to circumvent obstacles*. bioRxiv.

Small, J. V., Stradal, T., Vignal, E., and Rottner, K. (2002). The lamellipodium: Where motility begins. *Trends Cell Biol.* 12, 112–120. doi:10.1016/s0962-8924(01)02237-1

Sønder, S. L., Häger, S. C., Heitmann, A. S. B., Frankel, L. B., Dias, C., Simonsen, A. C., et al. (2021). Restructuring of the plasma membrane upon damage by lc3-associated macropinocytosis. *Sci. Adv.* 7, eabg1969. doi:10.1126/sciadv.abg1969

Suetsugu, S., Murayama, K., Sakamoto, A., Hanawa-Suetsugu, K., Seto, A., Oikawa, T., et al. (2006). The rac binding domain/irsp53-mim homology domain of irsp53 induces rac-dependent membrane deformation. *J. Biol. Chem.* 281, 35347–35358. doi:10.1074/jbc.M606814200

Svitkina, T. M. (2020). Actin cell cortex: Structure and molecular organization. *Trends Cell Biol.* 30, 556–565. doi:10.1016/j.tcb.2020.03.005

Takenawa, T., and Suetsugu, S. (2007). The wasp–wave protein network: Connecting the membrane to the cytoskeleton. *Nat. Rev. Mol. Cell Biol.* 8, 37–48. doi:10.1038/nrm2069

Theodorou, D. N., and Suter, U. W. (1985). Shape of unperturbed linear polymers: Polypropylene. *Macromolecules* 18, 1206–1214. doi:10.1021/ma00148a028

Tsai, F. C., Henderson, J. M., Jarin, Z., Kremneva, E., Senju, Y., Pernier, J., et al. (2022). Activated i-bar irsp53 clustering controls the formation of vasp-actin–based membrane protrusions. *Sci. Adv.* 8, eabp8677. doi:10.1126/sciadv.abp8677

Tu, Y., Pal, K., Austin, J., and Wang, X. (2022). Filopodial adhesive force in discrete nodes revealed by integrin molecular tension imaging. *Curr. Biol.* 32, 4386–4396.e3. doi:10.1016/j.cub.2022.08.040

Vaggi, F., Disanza, A., Milanesi, F., Di Fiore, P. P., Menna, E., Matteoli, M., et al. (2011). The eps8/irsp53/vasp network differentially controls actin capping and bundling in filopodia formation. *PLoS Comput. Biol.* 7, e1002088. doi:10.1371/journal.pcbi.1002088

Vicsek, T., and Zafeiris, A. (2012). Collective motion. *Phys. Rep.* 517, 71–140. doi:10.1016/j.physrep.2012.03.004

Welch, M. D., and Mullins, R. D. (2002). Cellular control of actin nucleation. *Annu. Rev. Cell Dev. Biol.* 18, 247–288. doi:10.1146/annurev.cellbio.18.040202.112133

Xia, S., Lim, Y. B., Zhang, Z., Wang, Y., Zhang, S., Lim, C. T., et al. (2019). Nanoscale architecture of the cortical actin cytoskeleton in embryonic stem cells. *Cell Rep.* 28, 1251–1267. doi:10.1016/j.celrep.2019.06.089

Zimmerberg, J., and Kozlov, M. M. (2006). How proteins produce cellular membrane curvature. *Nat. Rev. Mol. Cell Biol.* 7, 9–19. doi:10.1038/nrm1784